



Josephson effect in junctions of conventional and topological superconductors

Alex Zazunov¹, Albert Iks¹, Miguel Alvarado², Alfredo Levy Yeyati² and Reinhold Egger^{*1}

Full Research Paper

Open Access

Address:

¹Institut für Theoretische Physik, Heinrich-Heine-Universität, D-40225 Düsseldorf, Germany and ²Departamento de Física Teórica de la Materia Condensada C-V, Condensed Matter Physics Center (IFIMAC) and Instituto Nicolás Cabrera, Universidad Autónoma de Madrid, E-28049 Madrid, Spain

Email:

Reinhold Egger* - egger@hhu.de

* Corresponding author

Keywords:

Andreev bound states; Josephson current–phase relation; Majorana zero modes; topological superconductivity

Beilstein J. Nanotechnol. **2018**, *9*, 1659–1676.

doi:10.3762/bjnano.9.158

Received: 30 January 2018

Accepted: 27 April 2018

Published: 06 June 2018

This article is part of the Thematic Series "Topological materials".

Associate Editor: J. M. van Ruitenbeek

© 2018 Zazunov et al.; licensee Beilstein-Institut.

License and terms: see end of document.

Abstract

We present a theoretical analysis of the equilibrium Josephson current-phase relation in hybrid devices made of conventional *s*-wave spin-singlet superconductors (S) and topological superconductor (TS) wires featuring Majorana end states. Using Green's function techniques, the topological superconductor is alternatively described by the low-energy continuum limit of a Kitaev chain or by a more microscopic spinful nanowire model. We show that for the simplest S–TS tunnel junction, only the *s*-wave pairing correlations in a spinful TS nanowire model can generate a Josephson effect. The critical current is much smaller in the topological regime and exhibits a kink-like dependence on the Zeeman field along the wire. When a correlated quantum dot (QD) in the magnetic regime is present in the junction region, however, the Josephson current becomes finite also in the deep topological phase as shown for the cotunneling regime and by a mean-field analysis. Remarkably, we find that the S–QD–TS setup can support φ_0 -junction behavior, where a finite supercurrent flows at vanishing phase difference. Finally, we also address a multi-terminal S–TS–S geometry, where the TS wire acts as tunable parity switch on the Andreev bound states in a superconducting atomic contact.

Introduction

The physics of topological superconductors (TSs) is being vigorously explored at present. After Kitaev [1] showed that a one-dimensional (1D) spinless fermionic lattice model with nearest-neighbor *p*-wave pairing ('Kitaev chain') features a topologically nontrivial phase with Majorana bound states (MBSs) at open boundaries, references [2,3] have pointed out that the physics of the Kitaev chain could be realized in

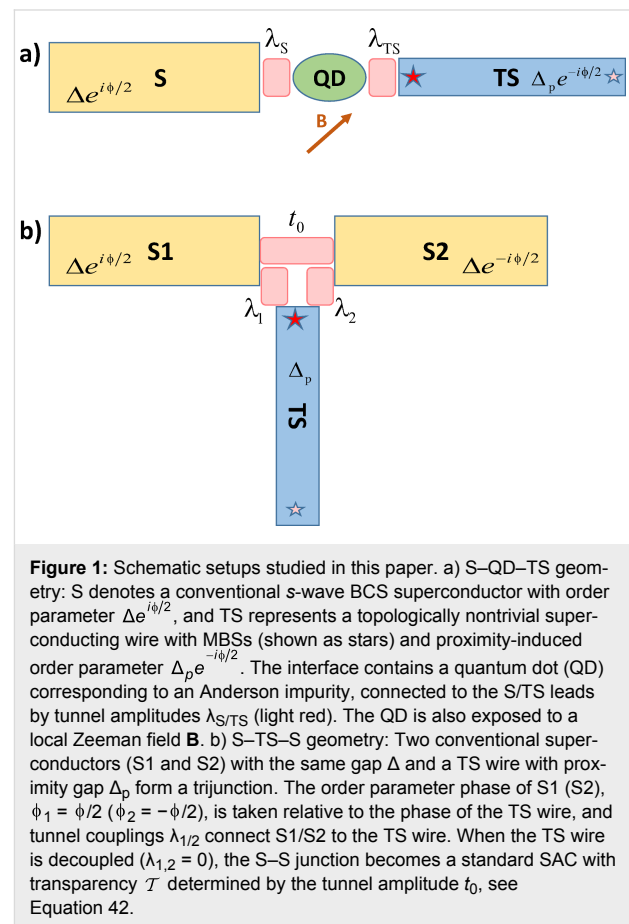
spin–orbit coupled nanowires with a magnetic Zeeman field and in the proximity to a nearby *s*-wave superconductor. The spinful nanowire model of references [2,3] indeed features *p*-wave pairing correlations for appropriately chosen model parameters. In addition, it also contains *s*-wave pairing correlations which become gradually smaller as one moves into the deep topological regime. Topologically nontrivial hybrid semiconductor

nanowire devices are of considerable interest in the context of quantum information processing [4-12], and they may also be designed in two-dimensional layouts by means of gate lithography techniques. Over the last few years, several experiments employing such platforms have provided mounting evidence for MBSs, e.g., from zero-bias conductance peaks in N–TS junctions (where N stands for a normal-conducting lead) and via signatures of the 4π -periodic Josephson effect in TS–TS junctions [13-25]. Related MBS phenomena have been reported for other material platforms as well [26-30], and most of the results reported below also apply to those settings. Available materials are often of sufficiently high quality to meet the conditions for ballistic transport, and we will therefore neglect disorder effects.

In view of the large amount of published theoretical works on the Josephson effect in such systems, let us first motivate the present study. (For a more detailed discussion and references, see below.) Our manuscript addresses the supercurrent flowing in Josephson junctions with a magnetic impurity. By considering Josephson junctions between a topological superconductor and a non-topological superconductor, we naturally extend previous works on Josephson junctions with a magnetic impurity between two conventional superconductors, as well as other works on Josephson junctions between topological and non-topological superconductors but without a magnetic impurity. In the simplest description, Josephson junctions between topological and non-topological superconductors carry no supercurrent. Instead, a supercurrent can flow only with certain deviations from the idealized model description. The presence of a magnetic impurity in the junction is one of these deviations, and this effect allows for novel signatures for the topological transition via the so-called φ_0 -behavior and/or through the kink-like dependence of the critical current on a Zeeman field driving the transition. We consider two different geometries in various regimes, e.g., the cotunneling regime where a controlled perturbation theory is possible, and a mean-field description of the stronger-coupling regime. We study both idealized Hamiltonians (allowing for analytical progress) as well as more realistic models for the superconductors.

To be more specific, we address the equilibrium current–phase relation (CPR) in different setups involving both conventional *s*-wave BCS superconductors (‘S’ leads) and TS wires, see Figure 1 for a schematic illustration. In general, the CPR is closely related to the Andreev bound state (ABS) spectrum of the system. For S–TS junctions with the TS wire deep in the topological phase such that it can be modeled by a Kitaev chain, the supercurrent vanishes identically [31]. This supercurrent blockade can be traced back to the different (*s/p*-wave) pairing symmetries for the S/TS leads, together with the fact that MBSs

have a definite spin polarization. For an early study of Josephson currents between superconductors with different (*p/d*) pairing symmetries, see also [32]. A related phenomenon concerns Multiple Andreev Reflection (MAR) features in nonequilibrium superconducting quantum transport at subgap voltages [33-36]. Indeed, it has been established that MAR processes are absent in S–TS junctions (with the TS wire in the deep topological regime) such that only quasiparticle transport above the gap is possible [37-44].



There are several ways to circumvent this supercurrent blockade in S–TS junctions. (i) One possibility has been described in [43]. For a trijunction formed by two TS wires and one S lead, crossed Andreev reflections allow for the nonlocal splitting of Cooper pairs in the S electrode involving both TS wires (or the reverse process). In this way, an equilibrium supercurrent will be generated unless the MBS spin polarization axes of both TS wires are precisely aligned. (ii) Even for a simple S–TS junction, a finite Josephson current is expected when the TS wire is modeled as spinful nanowire. This effect is due to the residual *s*-wave pairing character of the spinful TS model [2,3]. Interestingly, upon changing a control parameter, e.g., the bulk Zeeman field, which drives the TS wire across the topological phase

transition, we find that the critical current exhibits a kink-like feature that is mainly caused by a suppression of the Andreev state contribution in the topological phase. (iii) Yet another possibility is offered by junctions containing a magnetic impurity in a local magnetic field. We here analyze the S–QD–TS setup in Figure 1a in some detail, where a quantum dot (QD) is present within the S–TS junction region. The QD is modeled as an Anderson impurity [36], which is equivalent to a spin-1/2 quantum impurity over a wide parameter regime. Once spin mixing is induced by the magnetic impurity and the local magnetic field, we predict that a finite Josephson current flows even in the deep topological limit. In particular, in the cotunneling regime, we find an anomalous Josephson effect with finite supercurrent at vanishing phase difference (φ_0 -junction behavior) [45–47], see also [48–51]. The 2π -periodic CPR found in S–QD–TS junctions could thereby provide independent evidence for MBSs via the anomalous Josephson effect. In addition, we compute the CPR within the mean-field approximation in order to go beyond perturbation theory in the tunnel couplings connecting the QD to the superconducting leads. Our mean-field analysis shows that the φ_0 -junction behavior is a generic feature for S–QD–TS devices in the topological regime which is not limited to the cotunneling regime.

In the final part of the paper, we turn to the three-terminal S–TS–S setup shown in Figure 1b, where the S–S junction by itself (with the TS wire decoupled) represents a standard superconducting atomic contact (SAC) with variable transparency of the weak link. Recent experiments have demonstrated that the many-body ABS configurations of a SAC can be probed and manipulated to high accuracy by microwave spectroscopy [52–54]. When the TS wire is coupled to the S–S junction, see Figure 1b, the Majorana end state acts as a parity switch on the ABS system of the SAC. This effect allows for additional functionalities in Andreev spectroscopy. We note that similar ideas have also been explored for TS–N–TS systems [55].

Results and Discussion

S–QD–TS junction

Model

Let us start with the case of an S–QD–TS junction, where an interacting spin-degenerate single-level quantum dot (QD) is sandwiched between a conventional *s*-wave superconductor (S) and a topological superconductor (TS). This geometry is shown in Figure 1a. The corresponding topologically trivial S–QD–S problem has been studied in great detail over the past decades both theoretically [56–63] and experimentally [64–69]. A main motivation for those studies came from the fact that the QD can be driven into the magnetic regime where it represents a spin-1/2 impurity subject to Kondo screening by the leads. The Kondo effect then competes against the superconducting bulk

gap and one encounters local quantum phase transitions. By now, good agreement between experiment and theory has been established. Rather than studying the fate of the Kondo effect in the S–QD–TS setting of Figure 1a, we here pursue two more modest goals. First, we shall discuss the cotunneling regime in detail, where one can employ perturbation theory in the dot–lead couplings. This regime exhibits π -junction behavior in the S–QD–S case [56]. Second, in order to go beyond the cotunneling regime, we have performed a mean-field analysis similar in spirit to earlier work for S–QD–S devices [57,58].

The Hamiltonian for the setup in Figure 1a is given by

$$H = H_S + H_{TS} + H_{QD} + H_{\text{tun}}, \quad (1)$$

where $H_{S/TS}$ and H_{QD} describe the semi-infinite S/TS leads and the isolated dot in between, respectively, and H_{tun} refers to the tunnel contacts. We often use units with $e = \hbar = k_B = 1$, and $\beta = 1/T$ denotes inverse temperature. The QD is modeled as an Anderson impurity [36], i.e., a single spin-degenerate level of energy ε_0 with repulsive on-site interaction energy $U > 0$,

$$H_{QD} = \sum_{\sigma=\uparrow,\downarrow} \varepsilon_0 \left(n_\sigma - \frac{1}{2} \right) + U n_\uparrow n_\downarrow - \mathbf{B} \cdot \mathbf{S}, \quad (2)$$

where the QD occupation numbers are $n_\sigma = d_\sigma^\dagger d_\sigma = 0, 1$, with dot fermion operators d_σ and d_σ^\dagger for spin σ . Using standard Pauli matrices $\sigma_{x,y,z}$, we define

$$\mathbf{S}_{i=x,y,z} = \sum_{\sigma,\sigma'} d_\sigma^\dagger (\sigma_i)_{\sigma\sigma'} d_{\sigma'}, \quad (3)$$

such that $\mathbf{S}/2$ is a spin-1/2 operator. In the setup of Figure 1a, we also take into account an external Zeeman field $\mathbf{B} = (B_x, B_y, B_z)$ acting on the QD spin, where the units in Equation 2 include gyromagnetic and Bohr magneton factors. The spinful nanowire proposal for TS wires [2,3] also requires a sufficiently strong bulk Zeeman field oriented along the wire in order to realize the topologically nontrivial phase, but for concreteness, we here imagine the field \mathbf{B} as independent local field coupled only to the QD spin. One could use, e.g., a ferromagnetic grain near the QD to generate it. This field here plays a crucial role because for $\mathbf{B} = 0$, the S+QD part is spin rotation [SU(2)] invariant and the arguments of [31] then rule out a supercurrent for TS wires in the deep topological regime. We show below that unless \mathbf{B} is inadvertently aligned with the MBS spin polarization axis, spin mixing will indeed generate a supercurrent.

The S/TS leads are coupled to the QD via a tunneling Hamiltonian [70],

$$H_{\text{tun}} = \lambda_S \sum_{\sigma=\uparrow,\downarrow} \Psi_{\sigma}^{\dagger} d_{\sigma} + \lambda_{\text{TS}} e^{-i\phi/2} \Psi^{\dagger} d_{\uparrow} + \text{h.c.}, \quad (4)$$

where ψ_{σ} and ψ are boundary fermion fields representing the S lead and the effectively spinless TS lead, respectively. For the S lead, we assume the usual BCS model [62], where the operator ψ_{σ} annihilates an electron with spin σ at the junction. The TS wire will, for the moment, be described by the low-energy Hamiltonian of a Kitaev chain in the deep topological phase with chemical potential $\mu = 0$ [1,5]. The corresponding fermion operator ψ at the junction includes both the MBS contribution and above-gap quasiparticles [40]. Without loss of generality, we choose the unit vector \hat{e}_z as the MBS spin polarization direction and take real-valued tunnel amplitudes $\lambda_{\text{S/TS}}$, see Figure 1a, using a gauge where the superconducting phase difference ϕ appears via the QD–TS tunneling term. These tunnel amplitudes contain density-of-states factors for the respective leads. The operator expression for the current flowing through the system is then given by

$$\hat{I} = \frac{2e}{\hbar} \partial_{\phi} H_{\text{tun}}. \quad (5)$$

We do not specify $H_{\text{S/TS}}$ in Equation 1 explicitly since within the imaginary-time (τ) boundary Green's function (bGF) formalism [40] employed here, we only need to know the bGFs. For the S lead with gap value Δ , the bGF has the Nambu matrix form [40]

$$g(\tau) = -\langle \mathcal{T}_{\tau} \Psi_{\text{S}}(\tau) \Psi_{\text{S}}^{\dagger}(0) \rangle_0 = \beta^{-1} \sum_{\omega} e^{-i\omega\tau} g(\omega),$$

$$\Psi_{\text{S}} = \begin{pmatrix} \Psi_{\uparrow} \\ \Psi_{\downarrow} \end{pmatrix}, \quad g(\omega) = -\frac{i\omega\tau_0 + \Delta\tau_x}{\sqrt{\omega^2 + \Delta^2}}, \quad (6)$$

where the expectation value $\langle \dots \rangle_0$ refers to an isolated S lead, \mathcal{T} denotes time ordering, ω runs over fermionic Matsubara frequencies, i.e., $\omega = 2\pi(n + 1/2)/\beta$ with integer n , and we define Pauli (unity) matrices $\tau_{x,y,z}$ (τ_0) in particle–hole space corresponding to the Nambu spinor Ψ_{S} . Similarly, for a TS lead with proximity-induced gap Δ_{p} , the low-energy limit of a Kitaev chain yields the bGF [40]

$$G(\tau) = -\langle \mathcal{T}_{\tau} \Psi_{\text{TS}}(\tau) \Psi_{\text{TS}}^{\dagger}(0) \rangle_0, \quad \Psi_{\text{TS}} = \begin{pmatrix} \Psi \\ \Psi^{\dagger} \end{pmatrix}, \quad (7)$$

$$G(\omega) = \frac{1}{i\omega} \left(\sqrt{\omega^2 + \Delta_{\text{p}}^2} \tau_0 + \Delta_{\text{p}} \tau_x \right).$$

The matrices $\tau_{0,x}$ here act in the Nambu space defined by the spinor Ψ_{TS} . Later on we will address how our results change

when the TS wire is modeled as spinful nanowire [2,3], where the corresponding bGF has been specified in [43]. We emphasize that the bGF (Equation 7) captures the effects of both the MBS (via the $1/\omega$ term) and of the above-gap continuum quasiparticles (via the square root) [40,71].

In most of the following discussion, we will assume that U is the dominant energy scale, with the single-particle level located at $\varepsilon_0 \approx -U/2$. In that case, low-energy states with energy well below U are restricted to the single occupancy sector,

$$n_{\uparrow} + n_{\downarrow} = 1, \quad (8)$$

and the QD degrees of freedom become equivalent to the spin-1/2 operator $\mathbf{S}/2$ in Equation 3. In this regime, the QD acts like a magnetic impurity embedded in the S–TS junction. Using a Schrieffer–Wolff transformation to project the full Hamiltonian to the Hilbert subspace satisfying Equation 8, $H \rightarrow H_{\text{eff}}$, one arrives at the effective low-energy Hamiltonian

$$H_{\text{eff}} = H_0 + H_{\text{int}}, \quad H_0 = H_{\text{S}} + H_{\text{TS}} - \mathbf{B} \cdot \mathbf{S}, \quad (9)$$

with the interaction term

$$H_{\text{int}} = -\frac{2}{U} \sum_{\sigma,\sigma'} \left(\eta_{\sigma}^{\dagger} d_{\sigma} d_{\sigma'}^{\dagger} \eta_{\sigma'} + \text{h.c.} \right)$$

$$= \frac{2}{U} \sum_{\sigma=\uparrow/\downarrow=\pm} \left(\sigma S_z \eta_{\sigma}^{\dagger} \eta_{\sigma} + S_x \eta_{-\sigma}^{\dagger} \eta_{\sigma} \right) \quad (10)$$

$$+ \frac{2}{U} \delta n \sum_{\sigma} \eta_{\sigma}^{\dagger} \eta_{\sigma} - \frac{2\Lambda}{U} (\delta n + 1),$$

where $S_{\pm} = S_x \pm iS_y$, and $\delta n = \sum_{\sigma} n_{\sigma} - 1$. Moreover, $\Lambda = [\eta_{\sigma}, \eta_{\sigma}^{\dagger}]_{+}$ is the anticommutator of the composite boundary fields

$$\eta_{\sigma} = \lambda_{\text{S}} \Psi_{\sigma} + \delta_{\sigma,\uparrow} \lambda_{\text{TS}} e^{i\phi/2} \Psi. \quad (11)$$

We note that Λ is real-valued and does not depend on ϕ . Due to the constraint (Equation 8) on the dot occupation, the last two terms in Equation 10 do not contribute to the system dynamics and we obtain

$$H_{\text{int}} = \frac{4}{U} \sum_{\sigma,\sigma'} Q_{\sigma\sigma'} \eta_{\sigma}^{\dagger} \eta_{\sigma'}, \quad (12)$$

$$Q_{\sigma\sigma} = \frac{\sigma}{2} S_z, \quad Q_{\sigma,-\sigma} = \frac{1}{2} S_{-\sigma}.$$

A formally exact expression for the partition function is then given by

$$Z = \text{Tr}|_{\delta n=0} \left(e^{-\beta H_0} \mathcal{T}_\tau e^{-\int_0^\beta d\tau H_{\text{int}}(\tau)} \right), \quad (13)$$

where $H_{\text{int}}(\tau) = e^{\tau H_0} H_{\text{int}} e^{-\tau H_0}$ with H_0 in Equation 9 and the trace extends only over the Hilbert subspace corresponding to Equation 8. We can equivalently write Equation 13 in the form

$$\begin{aligned} Z &= Z_0 \left\langle \mathcal{T}_\tau e^{-\beta \hat{W}} \right\rangle_0 = e^{-\beta F}, \\ \hat{W} &= \beta^{-1} \int_0^\beta d\tau H_{\text{int}}(\tau), \\ Z_0 &= \text{Tr}|_{\delta n=0} e^{-\beta H_0} = e^{-\beta F_0}, \end{aligned} \quad (14)$$

where F is the free energy. The Josephson current then follows as $I = (2e/\hbar) \partial_\phi F$, see Equation 5.

Cotunneling regime

We now address the CPR in the elastic cotunneling regime,

$$\lambda_S \lambda_{\text{TS}} \ll \min\{\Delta, \Delta_p, U\}, \quad (15)$$

where perturbation theory in H_{int} is justified. We thus wish to compute the free energy $F(\phi)$ from Equation 14 to lowest nontrivial order. With $W_0 = \langle \hat{W} \rangle_0$, the standard cumulant expansion gives

$$F - F_0 = W_0 - \frac{\beta}{2} \left(\langle \hat{W}^2 \rangle_0 - W_0^2 \right) + \mathcal{O}(W)^2. \quad (16)$$

By virtue of Wick’s theorem, time-ordered correlation functions of the boundary operators (Equation 11) are now expressed in terms of S/TS bGF matrix elements, see Equation 6 and Equation 7,

$$\left\langle \mathcal{T}_\tau \eta_\sigma(\tau) \eta_{\sigma'}^\dagger(0) \right\rangle_0 = \delta_{\sigma\sigma'} \left[\lambda_S^2 \left\langle \mathcal{T}_\tau \Psi_\sigma(\tau) \Psi_\sigma^\dagger(0) \right\rangle_0 + \delta_{\sigma,\uparrow} \lambda_{\text{TS}}^2 \left\langle \mathcal{T}_\tau \Psi(\tau) \Psi^\dagger(0) \right\rangle_0 \right] \quad (17)$$

and similarly

$$\begin{aligned} \left\langle \mathcal{T}_\tau \eta_\sigma(\tau) \eta_{\sigma'}(0) \right\rangle_0 &= \delta_{\sigma,-\sigma'} \lambda_S^2 \left\langle \mathcal{T}_\tau \Psi_\sigma(\tau) \Psi_{-\sigma}(0) \right\rangle_0 \\ &+ e^{i\phi} \delta_{\sigma,\uparrow} \delta_{\sigma',\uparrow} \lambda_{\text{TS}}^2 \left\langle \mathcal{T}_\tau \Psi(\tau) \Psi(0) \right\rangle_0. \end{aligned} \quad (18)$$

Next we observe that $\partial_\phi \langle H_{\text{int}} \rangle_0 = 0$. As a consequence, the ϕ -independent terms W_0 and W_0^2 in Equation 16 do not contribute to the Josephson current. The leading contribution is then of second order in H_{int} ,

$$\begin{aligned} I(\phi) &= -\beta^{-1} \partial_\phi \int_0^\beta d\tau_1 d\tau_2 \left\langle \mathcal{T}_\tau H_{\text{int}}(\tau_1) H_{\text{int}}(\tau_2) \right\rangle_0 \\ &= -\frac{\kappa^2}{\beta} \int_0^\beta d\tau_1 d\tau_2 g_{12}(\tau_1 - \tau_2) G_{12}(\tau_1 - \tau_2) \\ &\times i e^{i\phi} \sum_\sigma \left\langle \mathcal{T}_\tau \mathcal{Q}_{\sigma,\uparrow}(\tau_1) \mathcal{Q}_{-\sigma,\uparrow}(\tau_2) \right\rangle_0 + \text{h.c.}, \end{aligned} \quad (19)$$

with $\mathcal{Q}_{\sigma,\sigma'}$ in Equation 12 and the small dimensionless parameter

$$\kappa = \frac{4\lambda_S \lambda_{\text{TS}}}{U} \ll 1. \quad (20)$$

From Equation 6 and Equation 7, the bGF matrix elements needed in Equation 19 follow as

$$\begin{aligned} g_{12}(\tau) &= -\frac{\Delta}{\beta} \sum_\omega \frac{\cos(\omega\tau)}{\sqrt{\omega^2 + \Delta^2}}, \\ G_{12}(\tau) &= -\frac{\Delta_p}{\beta} \sum_\omega \frac{\sin(\omega\tau)}{\omega} = -\frac{\Delta_p}{2} \text{sgn}(\tau). \end{aligned} \quad (21)$$

Now $|g_{12}(\tau)|$ is exponentially small unless $\Delta|\tau| < 1$. In particular, $g_{12}(\tau) \rightarrow -\delta(\tau)$ for $\Delta \rightarrow \infty$. Moreover, for $B \ll \Delta$ with $B \equiv |\mathbf{B}|$, the magnetic impurity (S) dynamics will be slow on time scales of the order of $1/\Delta$. We may therefore approximate the spin–spin correlators in Equation 19 by their respective equal-time expressions,

$$\lim_{\tau_1 \rightarrow \tau_2} \left\langle \mathcal{T}_\tau \mathcal{Q}_{\sigma,\uparrow}(\tau_1) \mathcal{Q}_{-\sigma,\uparrow}(\tau_2) \right\rangle_0 = \frac{\sigma}{4} \text{sgn}(\tau_1 - \tau_2) \langle S_+ \tau_1 \rangle_0. \quad (22)$$

Inserting Equation 21 and Equation 22 into the expression for the supercurrent in Equation 19, the time integrations can be carried out analytically.

We obtain the CPR in the cotunneling regime as

$$\begin{aligned} I(\phi) &= I_x \sin \phi + I_y \cos \phi, \\ I_{x,y} &= \frac{e\kappa^2 \Delta_p}{2\hbar} \frac{B_{x,y}}{B} \tanh(\beta B), \end{aligned} \quad (23)$$

with κ in Equation 20. We note that while $I(\phi)$ is formally independent of Δ , the value of Δ must be sufficiently large to justify the steps leading to Equation 23. Remarkably, Equation 23 predicts anomalous supercurrents for the S–QD–TS setup, i.e., a finite Josephson current for vanishing phase difference ($\phi = 0$) [45,46,72]. One can equivalently view this effect as a φ_0 -shift in the CPR, $I(\phi) = I_c \sin(\phi + \varphi_0)$. An observation of this φ_0 -junction behavior could then provide additional evidence for MBSs (see also [47]), where Equation 23 shows that the local magnetic field is required to have a finite B_y -component with \hat{e}_z defining the MBS spin polarization direction. In particular, if \mathbf{B} is aligned with \hat{e}_z , the supercurrent in Equation 23 vanishes identically since s -wave Cooper pairs cannot tunnel from the S lead into the TS wire in the absence of spin flips [31]. Otherwise, the CPR is 2π -periodic and sensitive to the MBS through the peculiar dependence on the relative orientation between the MBS spin polarization (\hat{e}_z) and the local Zeeman field \mathbf{B} on the QD. The fact that $B_y \neq 0$ (rather than $B_x \neq 0$) is necessary to have $\varphi_0 \neq 0$ can be traced back to our choice of real-valued tunnel couplings. For tunable tunnel phases, also the field direction where one has $\varphi_0 = 0$ will vary accordingly.

Noting that the anomalous Josephson effect has recently been observed in S–QD–S devices [73], we expect that similar experimental techniques will allow to access the CPR (Equation 23). We mention in passing that previous work has also pointed out that experiments employing QDs between N (instead of S) leads and TS wires can probe nonlocal effects due to MBSs [12,16,74–78]. In our case, e.g., by variation of the field direction in the xy -plane, Equation 23 predicts a tunable anomalous supercurrent. We conclude that in the cotunneling regime, the π -junction behavior of S–QD–S devices is replaced by the more exotic physics of φ_0 -junctions in the S–QD–TS setting.

Mean-field approximation

Next we present a mean-field analysis of the Hamiltonian (Equation 1) which allows us to go beyond the perturbative cotunneling regime. For the corresponding S–QD–S case, see [58,79]. We note that a full solution of this interacting many-body problem requires a detailed numerical analysis using, e.g., the numerical renormalization group [60,61] or quantum Monte Carlo simulations [59,63], which is beyond the scope of the present work. We start by defining the GF of the QD,

$$G_d(\tau) = -\langle \mathcal{T}_\tau \Psi_d(\tau) \Psi_d^\dagger(0) \rangle, \quad \Psi_d^\dagger = (d_\uparrow^\dagger, d_\downarrow^\dagger, d_\downarrow^\dagger, -d_\uparrow^\dagger)^T. \quad (24)$$

Note that this notation introduces double counting, which implies that only half of the levels are physically independent. Of course, the results below take this issue into account.

With the above Nambu bi-spinor basis, the mean-field Hamiltonian has the 4×4 matrix representation

$$\mathcal{H}_{\text{MF}} = \begin{pmatrix} \varepsilon_\uparrow & \Delta_d & \alpha_d & 0 \\ \Delta_d^* & -\varepsilon_\downarrow & 0 & \alpha_d \\ \alpha_d^* & 0 & \varepsilon_\downarrow & \Delta_d \\ 0 & \alpha_d^* & \Delta_d^* & -\varepsilon_\uparrow \end{pmatrix}, \quad (25)$$

$$\varepsilon_\uparrow = \varepsilon_0 - B_z + U \langle n_\downarrow \rangle, \quad \varepsilon_\downarrow = \varepsilon_0 + B_z + U \langle n_\uparrow \rangle,$$

$$\alpha_d = B_x + iB_y - U \langle d_\downarrow^\dagger d_\uparrow \rangle, \quad \Delta_d = U \langle d_\downarrow d_\uparrow \rangle.$$

The mean-field parameters appearing in Equation 25 follow by solving the self-consistency equations

$$\langle n_\uparrow \rangle = \frac{1}{\beta} \sum_\omega G_{d,11}(\omega), \quad \langle n_\downarrow \rangle = \frac{1}{\beta} \sum_\omega G_{d,33}(\omega), \quad (26)$$

$$\langle d_\downarrow^\dagger d_\uparrow \rangle = \frac{1}{\beta} \sum_\omega G_{d,13}(\omega), \quad \langle d_\downarrow d_\uparrow \rangle = \frac{1}{\beta} \sum_\omega G_{d,21}(\omega),$$

where the mean-field approximation readily yields

$$G_d(\omega) = [i\omega - \mathcal{H}_{\text{MF}} - \Sigma_S(\omega) - \Sigma_{\text{TS}}(\omega)]^{-1}. \quad (27)$$

The self-energies $\Sigma_{\text{S/TS}}(\omega)$ due to the coupling of the QD to the S/TS leads have the matrix representation

$$\Sigma_S = \Gamma_S \begin{pmatrix} g_{11} & -g_{12} & 0 & 0 \\ -g_{21} & g_{22} & 0 & 0 \\ 0 & 0 & g_{11} & -g_{12} \\ 0 & 0 & -g_{21} & g_{22} \end{pmatrix} \quad (28)$$

and

$$\Sigma_{\text{TS}} = \Gamma_{\text{TS}} \begin{pmatrix} G_{11} & 0 & 0 & -G_{12}e^{i\phi} \\ 0 & 0 & 0 & 0 \\ 0 & 0 & 0 & 0 \\ -G_{21}e^{i\phi} & 0 & 0 & G_{22} \end{pmatrix} \quad (29)$$

with the hybridization parameters $\Gamma_{\text{S/TS}} = \lambda_{\text{S/TS}}^2$. The bGFs $g(\omega)$ and $G(\omega)$ have been defined in Equation 6 and Equation 7, respectively. Once a self-consistent solution to Equation 26 has been determined, which in general requires numerics, the Josephson current is obtained from Equation 5 as

$$I(\phi) = -\frac{e}{\hbar\beta} \sum_{\omega} \frac{\partial_{\phi} \det[G_d^{-1}(\omega)]}{\det[G_d^{-1}(\omega)]}. \quad (30)$$

In what follows, we study a setup with $\Delta_p = \Delta$ and consider the zero-temperature limit.

In order to compare our self-consistent mean-field results to the noninteracting case, let us briefly summarize analytical expressions for the $U = 0$ ABS spectrum in the atomic limit defined by $\Gamma_{S,TS} \ll \Delta$. First we notice that at low energy scales, the self-energy $\Sigma = \Sigma_S + \Sigma_{TS}$, see Equation 28 and Equation 29, simplifies to

$$\Sigma \simeq \begin{pmatrix} \frac{2\Delta}{i\omega} \Gamma_{TS} & -\Gamma_S & 0 & -\frac{2\Delta}{i\omega} \Gamma_{TS} e^{i\phi} \\ -\Gamma_S & 0 & 0 & 0 \\ 0 & 0 & 0 & -\Gamma_S \\ -\frac{2\Delta}{i\omega} \Gamma_{TS} e^{i\phi} & 0 & -\Gamma_S & \frac{2\Delta}{i\omega} \Gamma_{TS} \end{pmatrix} \quad (31)$$

The ABS spectrum of the S–QD–TS junction then follows by solving a determinantal equation, $\det[G_d^{-1}(\omega)] = 0$. One finds a zero-energy pole which is related to the MBS and results from the $1/\omega$ dependence of $\Sigma_{TS}(\omega)$. In addition, we get finite-energy subgap poles for

$$i\omega \equiv E_A^{(\sigma_1=\pm, \sigma_2=\pm)} = \sigma_1 \sqrt{\frac{b_0 + \sigma_2 \sqrt{b_0^2 + 4c_0}}{2}}, \quad (32)$$

with the notation

$$\begin{aligned} b_0 &= \varepsilon_{\downarrow}^2 + \varepsilon_{\uparrow}^2 + 4\Gamma_{TS}\Delta + 2\Gamma_S^2 + 2|\alpha_d|^2, \\ c_0 &= -4\Gamma_{TS}\Delta \left(\varepsilon_{\downarrow}^2 + \Gamma_S^2 + |\alpha_d|^2 \right) - \varepsilon_{\uparrow}^2 \varepsilon_{\downarrow}^2 \\ &\quad - \left(|\alpha_d|^2 - \Gamma_S^2 \right) \left(|\alpha_d|^2 - \Gamma_S^2 - \varepsilon_{\uparrow} \varepsilon_{\downarrow} \right) \\ &\quad + 8\Delta\Gamma_S\Gamma_{TS} \operatorname{Re}(\alpha_d e^{i\phi}). \end{aligned} \quad (33)$$

In Figure 2, numerically exact results for the $U = 0$ ABS spectrum are compared to the analytical prediction (Equation 32). We first notice that, as expected, Equation 32 accurately fits the numerical results in the atomic limit, see the left panel in Figure 2. Deviations can be observed for larger values of $\Gamma_{S,TS}/\Delta$. However, as shown in the right panel of Figure 2, rather good agreement is again obtained by rescaling Equation 32 with a constant factor of the order of $(1 + \Gamma_{S,TS}/\Delta)$. For finite B_y , we find (data not shown) that the phase-dependent ABS spectrum is shifted with respect to $\phi = 0$. In fact, since the phase dependence of the subgap states comes from the term $\operatorname{Re}(\alpha_d e^{i\phi})$ in the atomic limit, see Equation 25 and Equation 33, B_y can be fully accounted for in this limit by simply shifting $\phi \rightarrow \phi + \phi_0$. We thereby recover the ϕ_0 -junction behavior discussed before for the cotunneling regime, see Equation 23.

We next turn to self-consistent mean-field results for the phase-dependent ABS spectrum at finite U . Figure 3 shows the spectrum for the electron–hole symmetric case $\varepsilon_0 = -U/2$, with other parameters as in the right panel of Figure 2. For moderate interaction strength, e.g., taking $U = \Delta$ (left panel), we find that com-

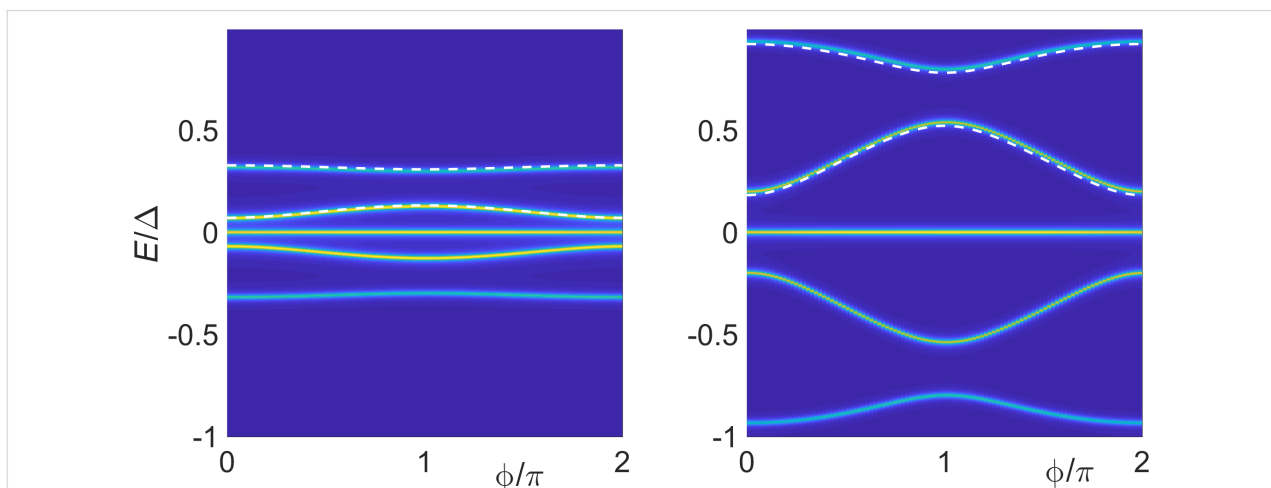
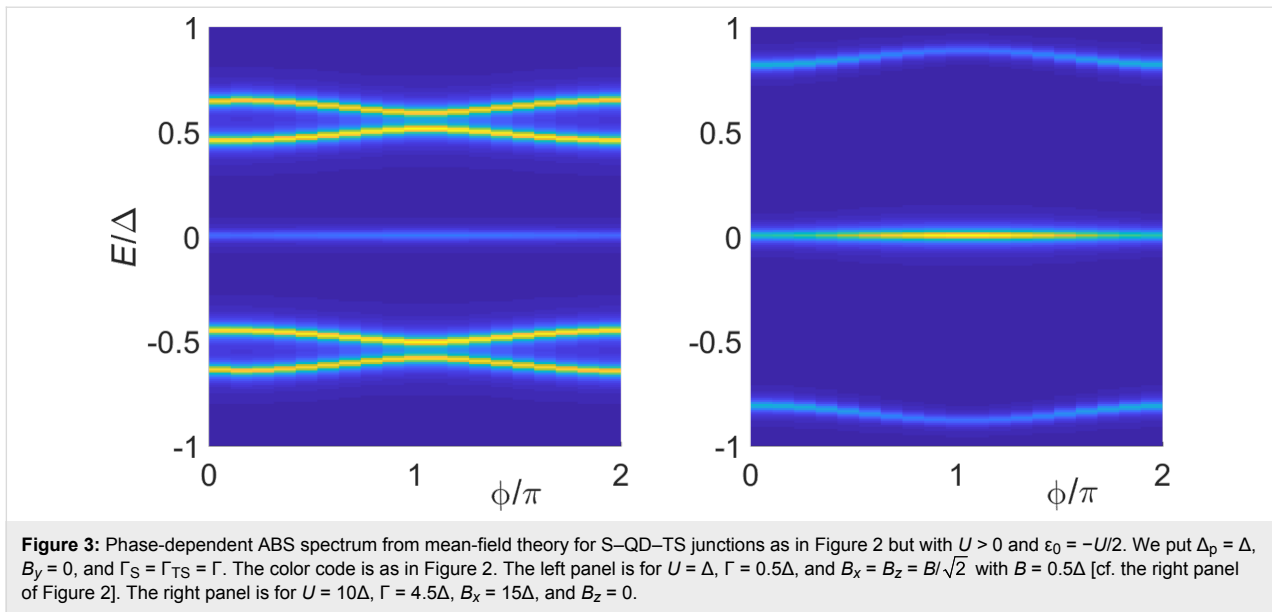


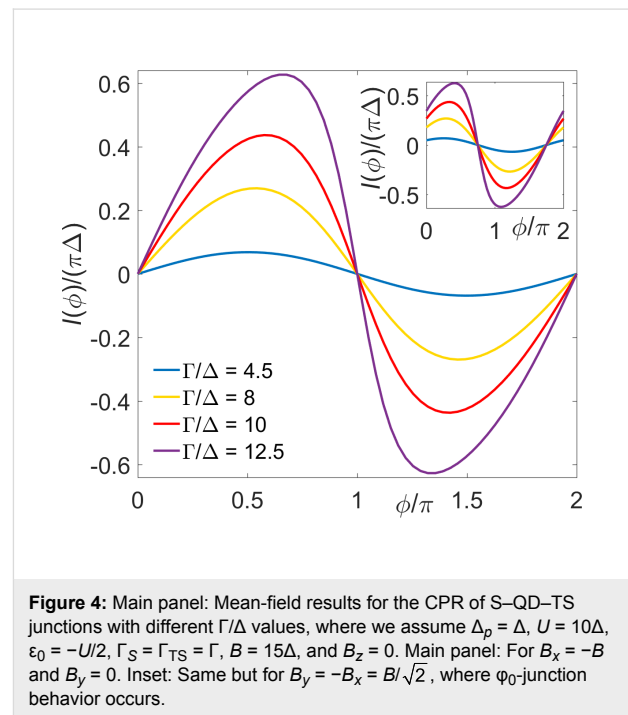
Figure 2: Phase dependence of the subgap spectrum of an S–QD–TS junction in the noninteracting case, $U = 0$. The TS wire is modeled from the low-energy limit of a Kitaev chain, and we use the parameters $B_y = 0$, $B_x = B_z = B/\sqrt{2}$, $\varepsilon_0 = 0$, $\Delta_p = \Delta$, and $\Gamma_S = \Gamma_{TS} = \Gamma$. From blue to yellow, the color code indicates increasing values of the spectral density. The left (right) panel is for $\Gamma = 0.045\Delta$ and $B = 0.1\Delta$ ($\Gamma = B = 0.5\Delta$). Solid curves were obtained by numerical evaluation of Equation 30. Dashed curves give the analytical prediction (Equation 32). In the right panel, the energies resulting from Equation 32 have been rescaled by the factor $1 + \Gamma/\Delta$.



pared to the $U = 0$ case in Figure 2, interactions push together pairs of Andreev bands, e.g., the pair corresponding to $E_A^{(+,\pm)}$ in Equation 30. On the other hand, for stronger interactions, e.g., $U = 10\Delta$ (right panel), the outer ABSs leak into the continuum spectrum and only the inner Andreev states remain inside the superconducting gap. The ABS spectrum shown in Figure 3 is similar to what is observed in mean-field calculations for S-QD-S systems with broken spin symmetry and in the magnetic regime of the QD, where one finds up to four ABSs for $U < \Delta$ while the outer ABSs merge with the continuum for $U > \Delta$ [79]. Interestingly, the inner ABS contribution to the free energy for $U = 10\Delta$ is minimal for $\phi = \pi$, see right panel of Figure 3, and we therefore expect π -junction behavior for $B_y = 0$ also in the regime with $U \gg \Delta$ and $B \gg \Delta$. We notice, however, that changing the sign of B_x would result in zero junction behavior. We interpret the inner ABSs for $U \gg \Delta$ as Shiba states with the phase dependence generated by the coupling to the MBS. Without the latter coupling, the Shiba state has ϕ -independent energy slightly below Δ determined by the scattering phase shift difference between both spin polarizations [80].

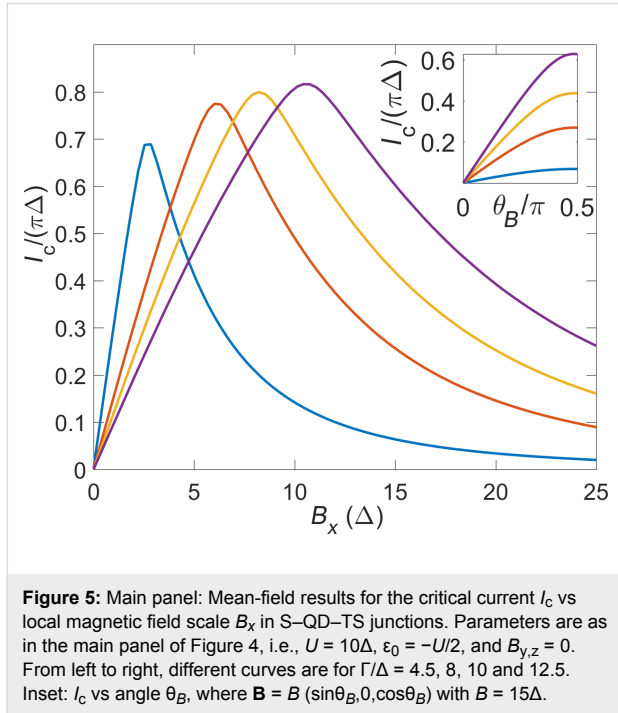
As illustrated in Figure 4, the CPR computed numerically from Equation 30 for different values of $\Gamma_{S,TS}/\Delta$, where B_x has been inverted with respect to its value in Figure 3, results in zero junction behavior. This behavior is expected from Equation 23 in the cotunneling regime, and Figure 4 shows that it also persists for $\Gamma_{S,TS} \gg \Delta$. In contrast to Equation 23, however, the CPR for $\Gamma_{S,TS} \gg \Delta$ differs from a purely sinusoidal behavior, see Figure 4. Moreover, for $B_y \neq 0$, we again encounter ϕ_0 -junction behavior, cf. the inset of Figure 4, in accordance with the perturbative result in Equation 23. Our mean-field results suggest that ϕ_0 -junction behavior is very robust and extends

also into other parameter regimes as long as the condition $B_y \neq 0$ is met.



Next, Figure 5 shows mean-field results for the critical current, $I_c = \max_\phi |I(\phi)|$, as function of the local magnetic field B_x and otherwise the same parameters as in Figure 4. The main panel in Figure 5 shows that I_c increases linearly with B_x for small $B_x < \Delta$, then exhibits a maximum around $B_x \approx \Gamma$, and subsequently decreases again to small values for $B_x \gg \max\{\Gamma_{S,TS}, \Delta\}$. On the other hand, for a fixed absolute

value B of the magnetic field and $B_y = 0$, the critical current also exhibits a maximum as a function of the angle θ_B between \mathbf{B} and the MBS spin polarization axis (\hat{e}_z). This effect is illustrated in the inset of Figure 5. As expected, the Josephson current vanishes for $\theta_B \rightarrow 0$, where the supercurrent blockade argument of [31] implies $I_c = 0$, and reaches its maximal value for $\theta_B = \pi/2$.



Spinful nanowire model for the TS Model

Before turning to the S-TS-S setup in Figure 1b, we address the question of how the above results for S-QD-TS junctions change when using the spinful nanowire model of [2,3] instead of the low-energy limit of a Kitaev chain, see Equation 7. In fact, we will first describe the Josephson current for the elementary case of an S-TS junction using the spinful nanowire model. Surprisingly, to the best of our knowledge, this case has not yet been addressed in the literature.

In spatially discretized form, the spinful nanowire model for TS wires reads [2,3,43]

$$H_{\text{TS}} = \frac{1}{2} \sum_j \left[\Psi_j^\dagger \hat{h} \Psi_j + \left(\Psi_j^\dagger \hat{t} \Psi_{j+1} + \text{h.c.} \right) \right], \quad (34)$$

$$\hat{h} = (2t - \mu) \tau_z \sigma_0 + V_x \tau_0 \sigma_x + \Delta_p \tau_x \sigma_0,$$

$$\hat{t} = -t \tau_z \sigma_0 + i\alpha \tau_z \sigma_z,$$

where the lattice fermion operators $c_{j\sigma}$ for given site j with spin polarizations $\sigma = \uparrow, \downarrow$ are combined to the four-spinor operator

$$\Psi_j = \left(c_{j\uparrow}, c_{j\downarrow}, c_{j\downarrow}^\dagger, -c_{j\uparrow}^\dagger \right)^T.$$

The Pauli matrices $\tau_{x,y,z}$ (and unity τ_0) again act in Nambu space, while Pauli matrices $\sigma_{x,y,z}$ and σ_0 refer to spin. In the figures shown below, we choose the model parameters in Equation 34 as discussed in [43]. The lattice spacing is set to $a = 10$ nm, which results in a nearest-neighbor hopping $t = \hbar^2/(2m^*a^2) = 20$ meV and the spin-orbit coupling strength $\alpha = 4$ meV for InAs nanowires. The proximity-induced pairing gap is again denoted by Δ_p , the chemical potential is μ , and the bulk Zeeman energy scale V_x is determined by a magnetic field applied along the wire. Under the condition

$$V_x > V_x^c = \sqrt{\mu^2 + \Delta_p^2}, \quad (35)$$

the topologically nontrivial phase is realized [2,3]. As we discuss below, the physics of the S-QD-TS junction sensitively depends on both the bulk Zeeman field V_x and on the local magnetic field \mathbf{B} acting on the QD, where one can either identify both magnetic fields or treat \mathbf{B} as independent field. In any case, the bGF $\tilde{G}(\omega)$ for the model in Equation 34, which now replaces the Kitaev chain result $G(\omega)$ in Equation 7, needs to be computed numerically. The bGF \tilde{G} has been described in detail in [43], where also a straightforward numerical scheme for calculating $\tilde{G}(\omega)$ has been devised. With the replacement $G \rightarrow \tilde{G}$, we can then take over the expressions for the Josephson current discussed before. Below we study these expressions in the zero-temperature limit.

S-TS junction

Let us first address the CPR for the S-TS junction case. The Josephson current can be computed using the bGF expression for tunnel junctions in [40], which is a simplified version of the above expressions for the S-QD-TS case. The spin-conserving tunnel coupling λ defines a transmission probability (transparency) \mathcal{T} of the normal junction [40,43]. Close to the topological transition, the transparency is well approximated by

$$\mathcal{T} = \frac{4(\lambda/t)^2}{\left[1 + (\lambda/t)^2\right]^2}, \quad (36)$$

where $t = 20$ meV is the hopping parameter in Equation 34. We then study the CPR and the resulting critical current I_c as a function of \mathcal{T} for both the topologically trivial ($V_x < V_x^c$) and the nontrivial ($V_x > V_x^c$) regime, see Equation 35.

In Figure 6, we show the V_x dependence of the critical current I_c for the symmetric case $\Delta = \Delta_p$. In particular, it is of interest to determine how I_c changes as one moves through the phase transition in Equation 35. First, we observe that I_c is strongly suppressed in the topological phase in comparison to the topologically trivial phase. In fact, I_c slowly decreases as one moves into the deep topological phase by increasing V_x . This observation is in accordance with the expected supercurrent blockade in the deep topological limit [31]: $I_c = 0$ for the corresponding Kitaev chain case since p -wave pairing correlations on the TS side are incompatible with s -wave correlations on the S side. However, a residual finite supercurrent can be observed even for rather large values of V_x . We attribute this effect to the remaining s -wave pairing correlations contained in the spinful nanowire model (Equation 34). Second, Figure 6 shows kink-like features in the $I_c(V_x)$ curve near the topological transition, $V_x \approx V_x^c$. The inset of Figure 6 demonstrates that this feature comes from a rapid decrease of the ABS contribution while the continuum contribution remains smooth. This observation suggests that continuum contributions in this setup mainly originate from s -wave pairing correlations which are not particularly sensitive to the topological transition.

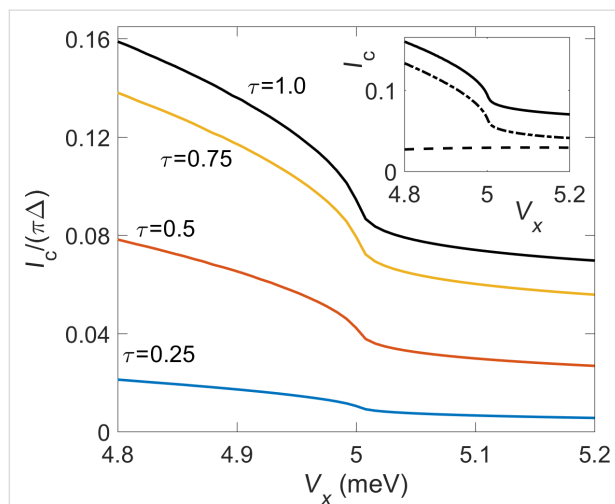


Figure 6: Main panel: Critical current I_c vs Zeeman energy V_x for an S–TS junction using the spinful TS nanowire model (Equation 34) for $\Delta_p = \Delta = 0.2$ meV, $\mu = 5$ meV, and different transparencies \mathcal{T} calculated from Equation 36. All other parameters are specified in the main text. Inset: Decomposition of I_c for $\mathcal{T} = 1$ into ABS (dotted-dashed) and continuum (dashed) contributions.

In Figure 7, we show the CPR for the S–TS junction with $\mathcal{T} = 1$ in Figure 6, where different curves correspond to differ-

ent Zeeman couplings V_x near the critical value. We find that in many parameter regions, in particular for $\mathcal{T} < 1$, the CPR is to high accuracy given by a conventional 2π -periodic Josephson relation, $I(\phi) = I_c \sin\phi$. In the topologically trivial phase, small deviations from the sinusoidal law can be detected, but once one enters the topological phase, these deviations become extremely small.

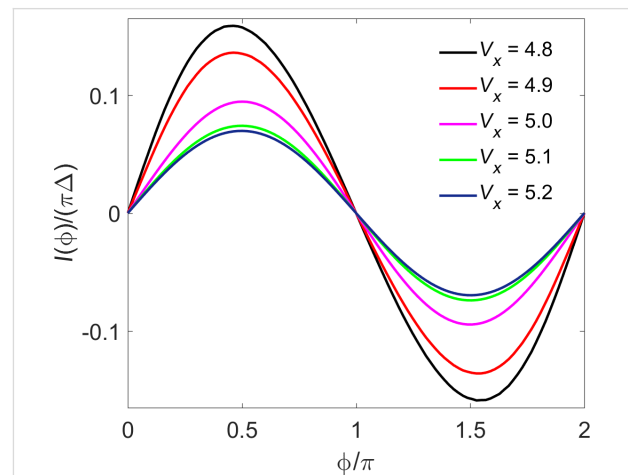


Figure 7: CPR for the S–TS junction with $\mathcal{T} = 1$ in Figure 6, for different bulk Zeeman fields V_x (in meV) near the critical value $V_x^c = 5.004$ meV.

S–QD–TS junction with spinful TS wire: Mean-field theory

Apart from providing a direct link to experimental control parameters, another advantage of using the spinful nanowire model of [2,3] for modeling the TS wire is that the angle between the local Zeeman field \mathbf{B} and the MBS spin polarization does not have to be introduced as phenomenological parameter but instead results from the calculation [43]. It is thus interesting to study the Josephson current in S–QD–TS junctions where the TS wire is described by the spinful nanowire model. For this purpose, we now revisit the mean-field scheme for S–QD–TS junctions using the bGF $\tilde{G}(\omega)$ for the spinful nanowire model (Equation 34). In particular, with the replacement $G \rightarrow \tilde{G}$, we solve the self-consistency equations (Equation 26) and thereby obtain the mean-field parameters in Equation 25. The resulting QD GF, $G_d(\omega)$ in Equation 27, then determines the Josephson current in Equation 30. Below we present self-consistent mean-field results obtained from this scheme. In view of the huge parameter space of this problem, we here only discuss a few key observations. A full discussion of the phase diagram and the corresponding physics will be given elsewhere.

The main panel of Figure 8 shows the critical current I_c vs the bulk Zeeman energy V_x for several values of the chemical potential μ , where the respective critical value V_x^c in

Equation 35 for the topological phase transition also changes with μ . The results in Figure 8 assume that the local magnetic field \mathbf{B} acting on the QD coincides with the bulk Zeeman field V_x in the TS wire, i.e., $\mathbf{B} = (V_x, 0, 0)$. For the rather large values of $\Gamma_{S,TS}$ taken in Figure 8, the I_c vs V_x curves again exhibit a kink-like feature near the topological transition, $V_x \approx V_x^c$. This behavior is very similar to what happens in S–TS junctions with large transparency \mathcal{T} , cf. Figure 6. As demonstrated in the inset of Figure 8, the physical reason for the kink feature can be traced back to a sudden drop of the ABS contribution to I_c when entering the topological phase $V_x > V_x^c$. In the latter phase, I_c becomes strongly suppressed in close analogy to the S–TS junction case shown in Figure 6.

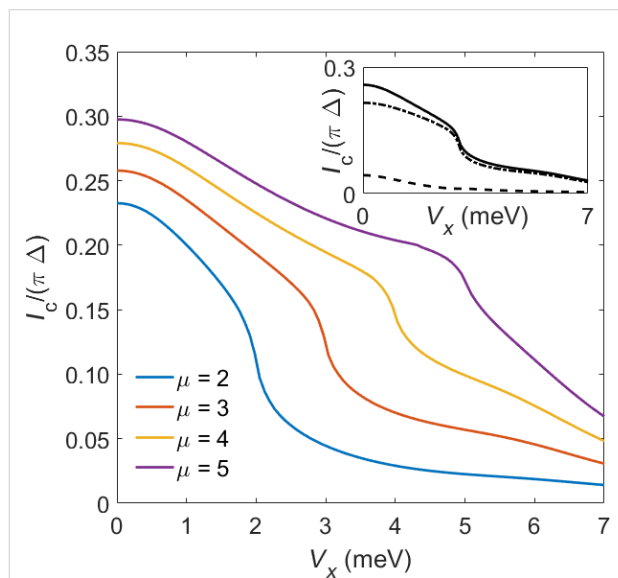


Figure 8: Main panel: Critical current I_c vs Zeeman energy V_x for S–QD–TS junctions from mean-field theory using the spinful TS nanowire model (Equation 34). Results are shown for several values of the chemical potential μ (in meV), where we assume $U = 10\Delta$, $\varepsilon_0 = -U/2$, $\Delta_p = \Delta = 0.2$ meV, $\Gamma_S = 2\Gamma_{TS} = 9\Delta$, and $\mathbf{B} = (V_x, 0, 0)$. Inset: Detailed view of the transition region $V_x \approx V_x^c$ for $\mu = 4$ meV, including a decomposition of I_c into the ABS (dotted-dashed) and the continuum (dashed) contribution.

In Figure 8, both the QD and the TS wire were subject to the same magnetic Zeeman field. If the direction and/or the size of the local magnetic field \mathbf{B} applied to the QD can be varied independently from the bulk magnetic field $V_x \hat{e}_x$ applied to the TS wire, one can arrive at rather different conclusions. To illustrate this statement, Figure 9 shows the I_c vs B_z dependence for $\mathbf{B} = (0, 0, B_z)$ perpendicular to the bulk field, with $V_x > V_x^c$ such that the TS wire is in the topological phase. In this case, Figure 9 shows that I_c exhibits a maximum close to $B_z \sim \Gamma$. This behavior is reminiscent of what we observed above in Figure 5, using the low-energy limit of a Kitaev chain for the bGF of the TS wire. Remarkably, the critical current can here reach values

close to the unitary limit, $I_c \sim e\Delta/\hbar$. We note that since B_z does not drive a phase transition, no kink-like features appear for the $I_c(B_z)$ curves shown in Figure 9. Finally, the inset of Figure 9 shows that for \mathbf{B} perpendicular to $V_x \hat{e}_x$, where $V_x > V_x^c$ for the parameters chosen in Figure 9, the ABSs provide the dominant contribution to the current in this regime.

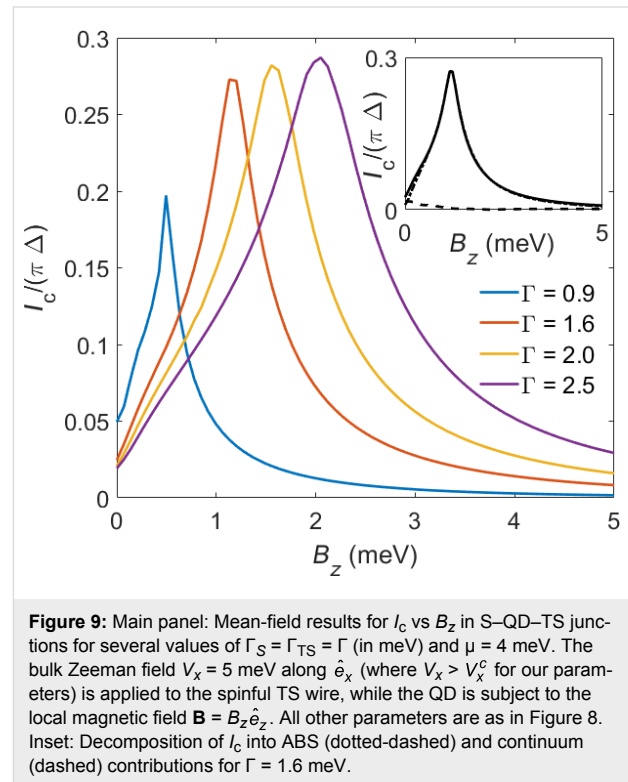


Figure 9: Main panel: Mean-field results for I_c vs B_z in S–QD–TS junctions for several values of $\Gamma_S = \Gamma_{TS} = \Gamma$ (in meV) and $\mu = 4$ meV. The bulk Zeeman field $V_x = 5$ meV along \hat{e}_x (where $V_x > V_x^c$ for our parameters) is applied to the spinful TS wire, while the QD is subject to the local magnetic field $\mathbf{B} = B_z \hat{e}_z$. All other parameters are as in Figure 8. Inset: Decomposition of I_c into ABS (dotted-dashed) and continuum (dashed) contributions for $\Gamma = 1.6$ meV.

S–TS–S junctions: Switching the parity of a superconducting atomic contact Model

We now proceed to the three-terminal S–TS–S setup shown in Figure 1b. The CPR found in the related TS–S–TS trijunction case has been discussed in detail in [43], see also [44]. Among other findings, a main conclusion of [43] for the TS–S–TS geometry was that the CPR can reveal information about the spin canting angle between the MBS spin polarization axes in both TS wires. In what follows, we study the superficially similar yet rather different case of an S–TS–S junction. Throughout this section, we model the TS wire via the low-energy theory of a spinless Kitaev chain, where the bGF $G(\omega)$ in Equation 7 applies.

One can view the setup in Figure 1b as a conventional superconducting atomic contact (SAC) with a TS wire tunnel-coupled to the S–S junction. Over the past few years, impressive experimental progress [52–54] has demonstrated that the ABS level system in a SAC [81] can be accurately probed and

manipulated by coherent or incoherent microwave spectroscopy techniques. We show below that an additional TS wire, cf. Figure 1b, acts as tunable parity switch on the many-body ABS levels of the SAC. As we have discussed above, the supercurrent flowing directly between a given S lead and the TS wire is expected to be strongly suppressed. However, through the hybridization with the MBS, Andreev level configurations with even and odd fermion parity are connected. This effect has profound and potentially useful consequences for Andreev spectroscopy.

An alternative view of the setup in Figure 1b is to imagine an S–TS junction, where S1 plays the role of the S lead and the spinful TS wire is effectively composed from a spinless (Kitaev) TS wire and the S2 superconductor. The p - and s -wave pairing correlations in the spinful TS wire are thereby spatially separated. Since the s - and p -wave bands represent normal modes, they are not directly coupled to each other in this scenario, i.e., we have to put $\lambda_2 = 0$. We discuss this analogy in more detail later on.

We consider a conventional single-channel SAC (gap Δ) coupled via a point contact to a TS wire (gap Δ_p), cf. Figure 1b. The superconducting phase difference across the SAC is denoted by $\phi = \phi_1 - \phi_2$, where ϕ_j is the phase difference between the respective S arm ($j = 1, 2$) and the TS wire. In practice, the SAC can be embedded into a superconducting ring for magnetic flux tuning of ϕ . To allow for analytical progress, we here assume that Δ_p is so large that continuum quasiparticle excitations in the TS wire can be neglected. In that case, only the MBS at the junction has to be kept when modeling the TS wire. However, we will also hint at how one can treat the general case.

For the two S leads, boundary fermion fields are contained in Nambu spinors as in Equation 6,

$$\Psi_{S,j=1,2} = \begin{pmatrix} \Psi_{j,\uparrow} \\ \Psi_{j,\downarrow}^\dagger \end{pmatrix}, \quad (37)$$

where their bGF follows with the Nambu matrix $g(\omega)$ in Equation 6 as

$$g_j^{-1}(\omega) = g^{-1}(\omega) + b_j \tau_0. \quad (38)$$

We again use Pauli matrices $\tau_{x,y,z}$ and unity τ_0 in Nambu space. The dimensionless parameters $b_{1,2}$ describe the Zeeman field component along the MBS spin polarization axis, see below. Since above-gap quasiparticles in the TS wire are neglected

here, the TS wire is represented by the Majorana operator $\gamma = \gamma^\dagger$, with $\gamma^2 = 1/2$, which anticommutes with all other fermions. We may represent γ by an auxiliary fermion f_\uparrow , where the index reminds us that the MBS spin polarization points along \hat{e}_z ,

$$\gamma = (f_\uparrow + f_\uparrow^\dagger) / \sqrt{2}. \quad (39)$$

The other Majorana mode $\gamma' = -i(f_\uparrow - f_\uparrow^\dagger) / \sqrt{2}$, which is localized at the opposite end of the TS wire, is assumed to have negligible hybridization with the $\Psi_{S,j}$ spinors and with γ . Writing the Euclidean action as $S = S_0 + S_{\text{tun}}$, we have an uncoupled action contribution,

$$S_0 = \sum_{j=1,2} \int_0^\beta d\tau d\tau' \bar{\Psi}_{S,j}(\tau) g_j^{-1}(\tau - \tau') \Psi_{S,j}(\tau') + \frac{1}{2} \int_0^\beta d\tau \gamma(\tau) \partial_\tau \gamma(\tau). \quad (40)$$

The leads are connected by a time-local tunnel action corresponding to the tunnel Hamiltonian

$$H_{\text{tun}} = t_0 \left(\Psi_{S,1}^\dagger \tau_z e^{i\tau_z \phi/2} \Psi_{S,2} + \text{h.c.} \right) + \sum_{j=1,2} \frac{\lambda_j}{\sqrt{2}} \left(\Psi_{j,\uparrow}^\dagger e^{i\phi_j/2} - \text{h.c.} \right) \gamma. \quad (41)$$

Without loss of generality, we assume that the tunnel amplitudes t_0 and $\lambda_{1,2}$, see Figure 1b, are real-valued and that they include density-of-state factors again. The parameter t_0 (with $0 \leq t_0 \leq 1$) determines the transparency \mathcal{T} of the SAC in the normal-conducting state [36], cf. Equation 36,

$$\mathcal{T} = \frac{4t_0^2}{(1+t_0^2)^2}. \quad (42)$$

Note that in Equation 41 we have again assumed spin-conserving tunneling, where only spin- \uparrow fermions in the SAC are tunnel-coupled to the Majorana fermion γ , cf. Equation 4.

At this stage, it is convenient to trace out the $\Psi_{S,2}$ spinor field. As a result, the SAC is described in terms of only one spinor field, $\Psi \equiv \Psi_{S,1}$, which however is still coupled to the Majorana field γ . After some algebra, we obtain the effective action

$$S_{\text{eff}} = \int_0^\beta d\tau d\tau' \left\{ \begin{array}{l} \bar{\Psi}(\tau) K^{-1}(\tau - \tau') \Psi(\tau') \\ + \Phi^T(\tau) \begin{bmatrix} \frac{1}{2} \delta(\tau - \tau') \partial_{\tau'} \\ -\lambda_2^2 P_\downarrow g_2(\tau - \tau') P_\uparrow \end{bmatrix} \Phi(\tau') \\ + \left[\begin{array}{l} \bar{\Psi}(\tau) \begin{pmatrix} \lambda_1 e^{i\phi_1/2} \delta(\tau - \tau') \\ -\lambda_2 e^{i\phi_2/2} t_0 \tau_z e^{i\tau_z \phi/2} g_2(\tau - \tau') \end{pmatrix} \\ P_\uparrow \Phi(\tau') + \text{h.c.} \end{array} \right] \end{array} \right\}, \quad (43)$$

where the operator $P_\uparrow = (\tau_0 + \tau_z)/2$ projects a Nambu spinor to its spin- \uparrow component. Moreover, we have defined an effective GF in Nambu space with frequency components

$$K^{-1}(\omega) = g_1^{-1}(\omega) - t_0^2 \tau_z e^{i\tau_z \phi/2} g_2(\omega) e^{-i\tau_z \phi/2} \tau_z, \quad (44)$$

and the TS lead has been represented by the Majorana–Nambu spinor

$$\Phi(\tau) = \frac{1}{\sqrt{2}} \begin{pmatrix} 1 \\ 1 \end{pmatrix} \gamma(\tau) = \tau_x \Phi^*(\tau). \quad (45)$$

We note in passing that Equation 43 could at this point be generalized to include continuum states in the TS wire. To that end, one has to (i) replace $\Phi \rightarrow (\psi, \psi^\dagger)^T$, where ψ is the boundary fermion of the effectively spinless TS wire, and (ii) replace $\delta(\tau - \tau') \partial_{\tau'} \rightarrow G^{-1}(\tau - \tau')$ with G in Equation 7. Including bulk TS quasiparticles becomes necessary for small values of the proximity gap, $\Delta_p \ll \Delta$, and/or when studying nonequilibrium applications within a Keldysh version of our formalism.

In any case, after neglecting the above-gap TS continuum quasiparticles, the partition function follows with S_{eff} in Equation 43 in the functional integral representation

$$Z = \int \mathcal{D}[\bar{\Psi}, \Psi, \gamma] e^{-S_{\text{eff}}} \equiv e^{-\beta F(\phi_1, \phi_2)}. \quad (46)$$

As before, the Josephson current through S lead no. j then follows from the free energy via

$$I_j = (2e/\hbar) \partial_{\phi_j} F.$$

The supercurrent flowing through the TS wire is then given by

$$I_{\text{TS}} = -(I_1 + I_2), \quad (47)$$

as dictated by current conservation.

Atomic limit

In order to get insight into the basic physics, we now analyze in detail the atomic limit, where Δ represents the largest energy scale of interest and hence the dynamics is confined to the subgap region. In this case, we can approximate $\sqrt{\Delta^2 + \omega^2} \approx \Delta$. After the rescaling

$$\Psi \rightarrow \sqrt{\Delta/(1+t_0^2)} \Psi$$

in Equation 43, we arrive at an effective action, $S_{\text{eff}} \rightarrow S_{\text{at}}$, valid in the atomic limit,

$$S_{\text{at}} = \int_0^\beta d\tau \left\{ \begin{array}{l} \frac{1}{2} \gamma \partial_\tau \gamma + \bar{\Psi} \begin{bmatrix} \partial_\tau + \Delta \cos(\phi/2) \tau_x \\ + r \Delta \sin(\phi/2) \tau_y + B_z \tau_0 \end{bmatrix} \Psi \\ + \frac{1}{\sqrt{2}} \sum_{\sigma=\uparrow, \downarrow} (\lambda_\sigma \Psi_\sigma^\dagger - \text{h.c.}) \gamma \end{array} \right\}, \quad (48)$$

where $r = \sqrt{1-T}$ is the reflection amplitude of the SAC, see Equation 42. We recall that $\Psi = (\psi_\uparrow, \psi_\downarrow)^T$, see Equation 37. Moreover, we define the auxiliary parameters

$$\begin{aligned} \lambda_\uparrow &= \lambda_1 \sqrt{(1+r)\Delta/2} e^{i\phi_1/2}, \\ \lambda_\downarrow &= -\lambda_2 \sqrt{(1-r)\Delta/2} e^{-i\phi_2/2}, \\ B_z &= \left(\frac{1+r}{2} b_1 + \frac{1-r}{2} b_2 \right) \Delta. \end{aligned} \quad (49)$$

The parameters $b_{1,2}$ in Equation 38 thus effectively generate the Zeeman scale B_z in Equation 49.

As a consequence of the atomic limit approximation, the action S_{at} in Equation 48 is equivalently expressed in terms of the effective Hamiltonian

$$\begin{aligned} H_{\text{at}} &= \sum_{\sigma=\uparrow, \downarrow} \sigma B_z \Psi_\sigma^\dagger \Psi_\sigma + \left(\delta_A \Psi_\uparrow^\dagger \Psi_\downarrow^\dagger + \text{h.c.} \right) \\ &+ \frac{1}{\sqrt{2}} \sum_{\sigma} (\lambda_\sigma \Psi_\sigma^\dagger - \text{h.c.}) \gamma, \end{aligned} \quad (50)$$

where we define

$$\delta_A(\phi) = \Delta [\cos(\phi/2) - ir \sin(\phi/2)]. \quad (51)$$

For a SAC decoupled from the TS wire and taken at zero field ($B_z = 0$), the ABS energy follows from Equation 50 in the standard form [62]

$$E_A(\phi) = |\delta_A| = \Delta \sqrt{1 - T \sin^2(\phi/2)}. \quad (52)$$

We emphasize that H_{at} neglects TS continuum quasiparticles as well as all types of quasiparticle poisoning processes. Let us briefly pause in order to make two remarks. First, we note that the Majorana field

$$\gamma = (f_{\uparrow} + f_{\uparrow}^{\dagger})/\sqrt{2},$$

see Equation 39, couples to both spin modes ψ_{σ} in Equation 50. The coupling λ_{\downarrow} between γ and the spin- \downarrow field in the SAC, ψ_{\downarrow} , is generated by crossed Andreev reflection processes, where a Cooper pair in lead S2 splits according to $\psi_{2,\uparrow}^{\dagger} \psi_{2,\downarrow}^{\dagger} \rightarrow f_{\uparrow}^{\dagger} \psi_{1,\downarrow}^{\dagger}$, plus the conjugate process. Second, we observe that H_{at} is invariant under a particle-hole transformation, amounting to the replacements $\psi_{\sigma} \rightarrow \psi_{\sigma}^{\dagger}$ and $f_{\uparrow} \rightarrow f_{\uparrow}^{\dagger}$, along with $B_z \rightarrow -B_z$ and $\phi_j \rightarrow 2\pi - \phi_j$.

We next notice that with $n_{\sigma} = \psi_{\sigma}^{\dagger} \psi_{\sigma} = 0, 1$ and $n_f = f_{\uparrow}^{\dagger} f_{\uparrow} = 0, 1$, the total fermion parity of the junction,

$$\mathcal{P}_{\text{tot}} = (-1)^{n_f + n_{\uparrow} + n_{\downarrow}} = \pm 1, \quad (53)$$

is a conserved quantity, $[\mathcal{P}_{\text{tot}}, H_{\text{at}}]_- = 0$. Below we restrict our analysis to the even-parity sector $\mathcal{P}_{\text{tot}} = +1$, but analogous results hold for the odd-parity case. The corresponding Hilbert subspace is spanned by four states,

$$|n_{\uparrow}, n_{\downarrow}, n_f\rangle = (\Psi_{\uparrow}^{\dagger})^{n_{\uparrow}} (\Psi_{\downarrow}^{\dagger})^{n_{\downarrow}} (f_{\uparrow}^{\dagger})^{n_f} |0\rangle, \quad (54)$$

where $(n_{\uparrow}, n_{\downarrow}, n_f) \in \{(0,0,0), (1,1,0), (1,0,1), (0,1,1)\}$ and $|0\rangle$ is the vacuum state. In this basis, the Hamiltonian (Equation 50) has the matrix representation

$$\mathcal{H}_{\text{at}}(\phi_1, \phi_2) = \begin{pmatrix} 0 & \delta_A^* & \lambda_{\uparrow}^*/2 & \lambda_{\downarrow}^*/2 \\ \delta_A & 0 & \lambda_{\downarrow}/2 & -\lambda_{\uparrow}/2 \\ \lambda_{\uparrow}/2 & \lambda_{\downarrow}^*/2 & B_z & 0 \\ \lambda_{\downarrow}/2 & -\lambda_{\uparrow}^*/2 & 0 & -B_z \end{pmatrix}. \quad (55)$$

The even-parity ground state energy, $E_G^{(e)} = \min(\epsilon)$, follows as the smallest root of the quartic equation

$$\det(\mathcal{H}_{\text{at}} - \epsilon) = 0. \quad (56)$$

In order to obtain simple results, let us now consider the special case $\lambda_2 = 0$, where the TS wire is directly coupled to lead S1 only, see Figure 1b. In that case, we also have $\lambda_{\downarrow} = 0$, see Equation 49, and Equation 56 implies the four eigenenergies $\pm \epsilon_{\pm}$ with

$$\epsilon_{\pm} = \frac{1}{\sqrt{2}} \left(\frac{E_A^2 + B_z^2 + \frac{1}{2} |\lambda_{\uparrow}|^2}{\pm \sqrt{(E_A^2 - B_z^2) + |\lambda_{\uparrow}|^2 (E_A^2 + B_z^2)}} \right)^{1/2}, \quad (57)$$

with $|\lambda_{\uparrow}|^2 = \lambda_1^2 (1+r)\Delta/2$, see Equation 49. The ground-state energy is thus given by $E_G^{(e)} = -\epsilon_{+}$. Since E_G depends on the phases $\phi_{1,2}$ only via the Andreev level energy $E_A(\phi)$ in Equation 52, the Josephson current through the SAC is given by

$$I_1 = -I_2 = \frac{2e}{\hbar} \partial_{\phi} E_G^{(e)} = -\frac{2e}{\hbar} \partial_{\phi} \epsilon_{+}. \quad (58)$$

Note that Equation 47 then implies that no supercurrent flows into the TS wire.

Next we observe that in the absence of the TS probe ($\lambda_1 = 0$), the even and odd fermion parity sectors of the SAC, $\mathcal{P}_{\text{SAC}} = (-1)^{n_{\uparrow} + n_{\downarrow}} = \pm 1$, are decoupled, see Equation 55, and Equation 57 yields $E_G^{(e)} = -\max(E_A, |B_z|)$. Importantly, the Josephson current is therefore fully blocked if the ground state is in the $\mathcal{P}_{\text{SAC}} = -1$ sector, i.e., for $|B_z| > E_A(\phi)$. For $\lambda_1 \neq 0$, however, \mathcal{P}_{SAC} is not conserved anymore. This implies that the MBS can act as parity switch between the two Andreev sectors with parity $\mathcal{P}_{\text{SAC}} = \pm 1$. Near the level crossing point at $E_A \approx |B_z|$, i.e., assuming $|E_A^2 - B_z^2| \ll |\lambda_{\uparrow}|^2 \ll E_A^2 + B_z^2$, we obtain

$$\epsilon_{\pm} \approx \frac{1}{\sqrt{2}} \left(E_A^2 + B_z^2 \pm \lambda_1 \sqrt{2(1+r)\Delta(E_A^2 + B_z^2)} \right)^{1/2}, \quad (59)$$

which implies a nonvanishing supercurrent through the SAC even in the field-dominated regime, $|B_z| > E_A$. The MBS therefore acts as a parity switch and leaves a trace in the CPR by lifting the supercurrent blockade.

Another interpretation

Interestingly, for $\lambda_2 = \phi_2 = 0$, the S–TS–S setup in Figure 1b could also be viewed as a toy model for an S–TS junction, where the TS part corresponds to a spinful model. In that analogy, the Nambu spinor $\Psi_{S,1}$ stands for the S lead while the spinful TS wire is represented by (i) the Nambu spinor $\Psi_{S,2}$ which is responsible for the residual s -wave pairing correlations, and (ii) by the MF γ (or, more generally, by the Kitaev-chain spinless boundary fermion ψ) which encodes p -wave pairing correlations. Moreover, t_0 and λ_1 should now be understood as spin-conserving phenomenological tunnel couplings acting in the s – s and s – p wave channels, respectively. The phase difference across this effective S–TS junction is $\phi = \phi_1$ and the net S–TS tunnel coupling is given by $\lambda = \sqrt{t_0^2 + \lambda_1^2}$. Putting $\lambda_1 = 0$ in the topologically trivial phase of the TS wire, the Josephson current carried by Andreev states in the s – s channel is blocked when the ground state is in the odd parity sector of the SAC. For $\lambda_1 \neq 0$, the MBS-mediated switching between odd and even parity sectors will now be activated and thereby lift the supercurrent blockade.

Conventional midgap level

A similar behavior as predicted above for the MBS-induced parity switch between $\mathcal{P}_{SAC} = \pm 1$ sectors could also be expected from a conventional fermionic subgap state tunnel-coupled to the SAC. Such a subgap state may be represented, e.g., by a single-level quantum dot in the Coulomb blockade regime. In particular, for a midgap (zero-energy) level with the fermion operator d , the Hamiltonian H_{at} in Equation 50 has to be replaced with

$$\begin{aligned} \tilde{H}_{at} = & \sum_{\sigma=\uparrow,\downarrow=\pm} \sigma B_z \Psi_{\sigma}^{\dagger} \Psi_{\sigma} + (\delta_A \Psi_{\uparrow}^{\dagger} \Psi_{\downarrow}^{\dagger} + \text{h.c.}) \\ & + \sum_{\sigma} (\lambda_{\sigma} \Psi_{\sigma}^{\dagger} d + \text{h.c.}). \end{aligned} \quad (60)$$

In the even total parity basis (Equation 54), the matrix representation of the Hamiltonian is then instead of Equation 55 given by

$$\mathcal{H}_{at}(\phi_1, \phi_2) = \begin{pmatrix} 0 & \delta_A^* & 0 & 0 \\ \delta_A & 0 & \lambda_{\downarrow} & -\lambda_{\uparrow} \\ 0 & \lambda_{\downarrow}^* & B_z & 0 \\ 0 & -\lambda_{\uparrow}^* & 0 & -B_z \end{pmatrix}. \quad (61)$$

Assuming $|\lambda_{\uparrow}| = |\lambda_{\downarrow}| \equiv \lambda$, Equation 56 then yields the eigenenergies $\pm \varepsilon_{\pm}$ with

$$\varepsilon_{\pm} = \frac{1}{\sqrt{2}} \left(\frac{E_A^2 + B_z^2 + 2\lambda^2}{\pm \sqrt{(E_A^2 - B_z^2) + 4\lambda^2 (E_A^2 + B_z^2 + \lambda^2)}} \right)^{1/2}. \quad (62)$$

Remarkably, the ABS spectra in Equation 62 and Equation 57 are rather similar for $\lambda^2 = \max(E_A^2, B_z^2)$. However, the MBS will automatically be located at zero energy and thus represents a generic situation.

Conclusion

We close this paper by summarizing our main findings. We have studied the Josephson effect in different setups involving both conventional s -wave BCS superconductors (S leads) and topologically nontrivial 1D p -wave superconductors (TS leads) with Majorana end states. The TS wires have been described either by a spinless theory applicable in the deep topological regime, which has the advantage of allowing for analytical progress but makes it difficult to establish contact to experimental control parameters, or by a spinful nanowire model as suggested in [2,3]. We have employed a unified imaginary-time Green's function approach to analyze the equilibrium properties of such devices, but a Keldysh generalization is straightforward and allows one to study also nonequilibrium applications.

For S–TS tunnel junctions, we find that in the topological phase of the TS wire, the supercurrent is mainly carried by above-gap continuum contributions. We confirm the expected supercurrent blockade [31] in the deep topological regime (where the spinless theory is fully valid and thus no residual s -wave pairing exists), while for realistic parameters, a small but finite critical current is found. To good approximation, the Josephson current obeys the usual 2π -periodic sinusoidal current–phase relation. The dependence of the critical current on the bulk Zeeman field driving the TS wire through the topological phase transition shows a kink-like feature at the critical value, which is caused by a sudden drop of the Andreev state contribution.

The supercurrent blockade in the deep topological phase could be lifted by adding a magnetic impurity to the junction, also allowing for the presence of a local magnetic field \mathbf{B} . Such a magnetic impurity arises from a spin-degenerate quantum dot (QD), and we have studied the corresponding S–QD–TS problem for both the spinless and the spinful TS wire model. Based on analytical results valid in the cotunneling regime as well as numerical results within the mean-field approximation, we predict ϕ_0 -junction behavior (anomalous Josephson effect) for the current–phase relation when the TS wire is in the topological phase.

As a final example for devices combining conventional and topological superconductors, we have shown that S–TS–S devices allow for a Majorana-induced parity switch between Andreev state sectors with different parity in a superconducting atomic contact. This observation could be useful for future microwave spectroscopy experiments of Andreev qubits in such contacts.

Acknowledgements

We acknowledge funding by the Deutsche Forschungsgemeinschaft (Grant No. EG 96/11-1) and by the Spanish MINECO through Grant No. FIS2014-55486-P and through the “María de Maeztu” Programme for Units of Excellence in R&D (MDM-2014-0377).

References

- Kitaev, A. Yu. *Phys.-Usp.* **2001**, *44*, 131. doi:10.1070/1063-7869/44/10S/S29
- Lutchyn, R. M.; Sau, J. D.; Das Sarma, S. *Phys. Rev. Lett.* **2010**, *105*, 077001. doi:10.1103/physrevlett.105.077001
- Oreg, Y.; Refael, G.; von Oppen, F. *Phys. Rev. Lett.* **2010**, *105*, 177002. doi:10.1103/physrevlett.105.177002
- Alicea, J.; Oreg, Y.; Refael, G.; von Oppen, F.; Fisher, M. P. A. *Nat. Phys.* **2011**, *7*, 412. doi:10.1038/nphys1915
- Alicea, J. *Rep. Prog. Phys.* **2012**, *75*, 076501. doi:10.1088/0034-4885/75/7/076501
- Leijnse, M.; Flensberg, K. *Semicond. Sci. Technol.* **2012**, *27*, 124003. doi:10.1088/0268-1242/27/12/124003
- Beenakker, C. W. J. *Annu. Rev. Condens. Matter Phys.* **2013**, *4*, 113. doi:10.1146/annurev-conmatphys-030212-184337
- Aasen, D.; Hell, M.; Mishmash, R. V.; Higginbotham, A.; Danon, J.; Leijnse, M.; Jespersen, T. S.; Folk, J. A.; Marcus, C. M.; Flensberg, K.; Alicea, J. *Phys. Rev. X* **2016**, *6*, 031016. doi:10.1103/physrevx.6.031016
- Landau, L. A.; Plugge, S.; Sela, E.; Altland, A.; Albrecht, S. M.; Egger, R. *Phys. Rev. Lett.* **2016**, *116*, 050501. doi:10.1103/physrevlett.116.050501
- Plugge, S.; Landau, L. A.; Sela, E.; Altland, A.; Flensberg, K.; Egger, R. *Phys. Rev. B* **2016**, *94*, 174514. doi:10.1103/physrevb.94.174514
- Plugge, S.; Rasmussen, A.; Egger, R.; Flensberg, K. *New J. Phys.* **2017**, *19*, 012001. doi:10.1088/1367-2630/aa54e1
- Aguado, R. *Riv. Nuovo Cimento Soc. Ital. Fis.* **2017**, *40*, 523. doi:10.1393/ncr/i2017-10141-9
- Mourik, V.; Zuo, K.; Frolov, S. M.; Plissard, S. R.; Bakkers, E. P. A. M.; Kouwenhoven, L. P. *Science* **2012**, *336*, 1003. doi:10.1126/science.1222360
- Das, A.; Ronen, Y.; Most, Y.; Oreg, Y.; Heiblum, M.; Shtrikman, H. *Nat. Phys.* **2012**, *8*, 887. doi:10.1038/nphys2479
- Albrecht, S. M.; Higginbotham, A. P.; Madsen, M.; Kuemmeth, F.; Jespersen, T. S.; Nygård, J.; Krogstrup, P.; Marcus, C. M. *Nature* **2016**, *531*, 206. doi:10.1038/nature17162
- Deng, M. T.; Vaitiekėnas, S.; Hansen, E. B.; Danon, J.; Leijnse, M.; Flensberg, K.; Nygård, J.; Krogstrup, P.; Marcus, C. M. *Science* **2016**, *354*, 1557. doi:10.1126/science.aaf3961
- Gül, Ö.; Zhang, H.; de Vries, F. K.; van Veen, J.; Zuo, K.; Mourik, V.; Conesa-Boj, S.; Nowak, M. P.; van Woerkom, D. J.; Quintero-Pérez, M.; Cassidy, M. C.; Geresdi, A.; Koelling, S.; Car, D.; Plissard, S. R.; Bakkers, E. P. A. M.; Kouwenhoven, L. P. *Nano Lett.* **2017**, *17*, 2690. doi:10.1021/acs.nanolett.7b00540
- Albrecht, S. M.; Hansen, E. B.; Higginbotham, A. P.; Kuemmeth, F.; Jespersen, T. S.; Nygård, J.; Krogstrup, P.; Danon, J.; Flensberg, K.; Marcus, C. M. *Phys. Rev. Lett.* **2017**, *118*, 137701. doi:10.1103/physrevlett.118.137701
- Zhang, H.; Gül, Ö.; Conesa-Boj, S.; Nowak, M. P.; Wimmer, M.; Zuo, K.; Mourik, V.; de Vries, F. K.; van Veen, J.; de Moor, M. W. A.; Bommer, J. D. S.; van Woerkom, D.; Car, D.; Plissard, S. R.; Bakkers, E. P. A. M.; Quintero-Pérez, M.; Cassidy, M. C.; Koelling, S.; Goswami, S.; Watanabe, K.; Taniguchi, T.; Kouwenhoven, L. P. *Nat. Commun.* **2017**, *8*, 16025. doi:10.1038/ncomms16025
- Nichele, F.; Drachmann, A. C. C.; Whiticar, A. M.; O’Farrell, E. C. T.; Suominen, H. J.; Fornieri, A.; Wang, T.; Gardner, G. C.; Thomas, C.; Hatke, A. T.; Krogstrup, P.; Manfra, M. J.; Flensberg, K.; Marcus, C. M. *Phys. Rev. Lett.* **2017**, *119*, 136803. doi:10.1103/physrevlett.119.136803
- Suominen, H. J.; Kjaergaard, M.; Hamilton, A. R.; Shabani, J.; Palmström, C. J.; Marcus, C. M.; Nichele, F. *Phys. Rev. Lett.* **2017**, *119*, 176805. doi:10.1103/physrevlett.119.176805
- Gazibegovich, S.; Car, D.; Zhang, H.; Balk, S. C.; Logan, J. A.; de Moor, M. W. A.; Cassidy, M. C.; Schmits, R.; Xu, D.; Wang, G.; Krogstrup, P.; Op het Veld, R. L. M.; Shen, J.; Bouman, D.; Shojaei, B.; Pennachio, D.; Lee, J. S.; van Veldhoven, P. J.; Koelling, S.; Verheijen, M. A.; Kouwenhoven, L. P.; Palmström, C. J.; Bakkers, E. P. A. M. *Nature* **2017**, *548*, 434. doi:10.1038/nature23468
- Zhang, H.; Liu, C.-X.; Gazibegovic, S.; Xu, D.; Logan, J. A.; Wang, G.; van Loo, N.; Bommer, J. D. S.; de Moor, M. W. A.; Car, D.; Op het Veld, R. L. M.; van Veldhoven, P. J.; Koelling, S.; Verheijen, M. A.; Pendharkar, M.; Pennachio, D. J.; Shojaei, B.; Lee, J. S.; Palmstrom, C. J.; Bakkers, E. P. A. M.; Das Sarma, S.; Kouwenhoven, L. P. *Nature* **2018**, *556*, 74–79. doi:10.1038/nature26142
- Deng, M. T.; Vaitiekėnas, S.; Prada, E.; San-José, P.; Nygård, J.; Krogstrup, P.; Aguado, R.; Marcus, C. M. *arXiv* **2017**, No. 1712.03536.
- Laroche, D.; Bouman, D.; van Woerkom, D. J.; Proutski, A.; Murthy, C.; Pikulin, D. I.; Nayak, C.; van Gulik, R. J. J.; Nygård, J.; Krogstrup, P.; Kouwenhoven, L. P.; Geresdi, A. *arXiv* **2017**, No. 1712.08459.
- Nadj-Perge, S.; Drozdov, I. K.; Li, J.; Chen, H.; Jeon, S.; Seo, J.; MacDonald, A. H.; Bernevig, B. A.; Yazdani, A. *Science* **2014**, *346*, 602. doi:10.1126/science.1259327
- Ruby, M.; Pientka, F.; Peng, Y.; von Oppen, F.; Heinrich, B. W.; Franke, K. J. *Phys. Rev. Lett.* **2015**, *115*, 197204. doi:10.1103/physrevlett.115.197204
- Sun, H.-H.; Zhang, K.-W.; Hu, L.-H.; Li, C.; Wang, G.-Y.; Ma, H.-Y.; Xu, Z.-A.; Gao, C.-L.; Guan, D.-D.; Li, Y.-Y.; Liu, C.; Qian, D.; Zhou, Y.; Fu, L.; Li, S.-C.; Zhang, F.-C.; Jia, J.-F. *Phys. Rev. Lett.* **2016**, *116*, 257003. doi:10.1103/physrevlett.116.257003
- Feldman, B. E.; Randeria, M. T.; Li, J.; Jeon, S.; Xie, Y.; Wang, Z.; Drozdov, I. K.; Andrei Bernevig, B.; Yazdani, A. *Nat. Phys.* **2017**, *13*, 286. doi:10.1038/nphys3947
- Deacon, R. S.; Wiedenmann, J.; Bocquillon, E.; Domínguez, F.; Klapwijk, T. M.; Leubner, P.; Brüne, C.; Hankiewicz, E. M.; Tarucha, S.; Ishibashi, K.; Buhmann, H.; Molenkamp, L. W. *Phys. Rev. X* **2017**, *7*, 021011. doi:10.1103/physrevx.7.021011
- Zazunov, A.; Egger, R. *Phys. Rev. B* **2012**, *85*, 104514. doi:10.1103/physrevb.85.104514

32. Kwon, H.-J.; Sengupta, K.; Yakovenko, V. M. *Eur. Phys. J. B* **2004**, *37*, 349. doi:10.1140/epjb/e2004-00066-4
33. Bratus, E. N.; Shumeiko, V. S.; Wendin, G. *Phys. Rev. Lett.* **1995**, *74*, 2110. doi:10.1103/physrevlett.74.2110
34. Averin, D.; Bardas, A. *Phys. Rev. Lett.* **1995**, *75*, 1831. doi:10.1103/physrevlett.75.1831
35. Cuevas, J. C.; Martín-Rodero, A.; Levy Yeyati, A. *Phys. Rev. B* **1996**, *54*, 7366. doi:10.1103/physrevb.54.7366
36. Nazarov, Y.; Blanter, Y. *Quantum Transport: Introduction to Nanoscience*; Cambridge University Press: Cambridge, United Kingdom, 2010.
37. Peng, Y.; Pientka, F.; Vinkler-Aviv, Y.; Glazman, L. I.; von Oppen, F. *Phys. Rev. Lett.* **2015**, *115*, 266804. doi:10.1103/physrevlett.115.266804
38. Ioselevich, P. A.; Ostrovsky, P. M.; Feigel'man, M. V. *Phys. Rev. B* **2016**, *93*, 125435. doi:10.1103/physrevb.93.125435
39. Sharma, G.; Tewari, S. *Phys. Rev. B* **2016**, *93*, 195161. doi:10.1103/physrevb.93.195161
40. Zazunov, A.; Egger, R.; Levy Yeyati, A. *Phys. Rev. B* **2016**, *94*, 014502. doi:10.1103/physrevb.94.014502
41. Setiawan, F.; Cole, W. S.; Sau, J. D.; Das Sarma, S. *Phys. Rev. B* **2017**, *95*, 174515. doi:10.1103/PhysRevB.95.174515
42. Setiawan, F.; Cole, W. S.; Sau, J. D.; Das Sarma, S. *Phys. Rev. B* **2017**, *95*, 020501. doi:10.1103/physrevb.95.020501
43. Zazunov, A.; Egger, R.; Alvarado, M.; Levy Yeyati, A. *Phys. Rev. B* **2017**, *96*, 024516. doi:10.1103/physrevb.96.024516
44. Deb, O.; Sengupta, K.; Sen, D. *arXiv* **2017**, No. 1712.03726.
45. Buzdin, A. *Phys. Rev. Lett.* **2008**, *101*, 107005. doi:10.1103/physrevlett.101.107005
46. Zazunov, A.; Egger, R.; Jonckheere, T.; Martin, T. *Phys. Rev. Lett.* **2009**, *103*, 147004. doi:10.1103/physrevlett.103.147004
47. Schrade, C.; Hoffman, S.; Loss, D. *Phys. Rev. B* **2017**, *95*, 195421. doi:10.1103/physrevb.95.195421
48. Yokoyama, T.; Eto, M.; Nazarov, Y. V. *Phys. Rev. B* **2014**, *89*, 195407. doi:10.1103/physrevb.89.195407
49. Camjayi, A.; Arrachea, L.; Aligia, A.; von Oppen, F. *Phys. Rev. Lett.* **2017**, *119*, 046801. doi:10.1103/physrevlett.119.046801
50. Cayao, J.; San-José, P.; Black-Schaffer, A. M.; Aguado, R.; Prada, E. *Phys. Rev. B* **2017**, *96*, 205425. doi:10.1103/physrevb.96.205425
51. Cayao, J.; San-José, P.; Black-Schaffer, A. M.; Prada, E.; Aguado, R. *arXiv* **2017**, No. 1712.08127.
52. Bretheau, L.; Girit, Ç. Ö.; Pothier, H.; Esteve, D.; Urbina, C. *Nature* **2013**, *499*, 312. doi:10.1038/nature12315
53. Bretheau, L.; Girit, Ç. Ö.; Urbina, C.; Esteve, D.; Pothier, H. *Phys. Rev. X* **2013**, *3*, 041034. doi:10.1103/physrevx.3.041034
54. Janvier, C.; Tosi, L.; Bretheau, L.; Girit, Ç. Ö.; Stern, M.; Bertet, P.; Joyez, P.; Vion, D.; Esteve, D.; Goffman, M. F.; Pothier, H.; Urbina, C. *Science* **2015**, *349*, 1199. doi:10.1126/science.aab2179
55. Tarasinski, B.; Chevallier, D.; Hutasoit, J. A.; Baxevaris, B.; Beenakker, C. W. J. *Phys. Rev. B* **2015**, *92*, 144306. doi:10.1103/physrevb.92.144306
56. Glazman, L. I.; Matveev, K. A. *JETP Lett.* **1989**, *49*, 659.
57. Rozhkov, A. V.; Arovas, D. P. *Phys. Rev. Lett.* **1999**, *82*, 2788. doi:10.1103/physrevlett.82.2788
58. Vecino, E.; Martín-Rodero, A.; Levy Yeyati, A. *Phys. Rev. B* **2003**, *68*, 035105. doi:10.1103/physrevb.68.035105
59. Siano, F.; Egger, R. *Phys. Rev. Lett.* **2004**, *93*, 047002. doi:10.1103/physrevlett.93.047002
60. Choi, M.-S.; Lee, M.; Kang, K.; Belzig, W. *Phys. Rev. B* **2004**, *70*, 020502. doi:10.1103/physrevb.70.020502
61. Karrasch, C.; Oguri, A.; Meden, V. *Phys. Rev. B* **2008**, *77*, 024517. doi:10.1103/physrevb.77.024517
62. Martín-Rodero, A.; Levi Yeyati, A. *Adv. Phys.* **2011**, *60*, 899. doi:10.1080/00018732.2011.624266
63. Luitz, D. J.; Assaad, F. F.; Novotný, T.; Karrasch, C.; Meden, V. *Phys. Rev. Lett.* **2012**, *108*, 227001. doi:10.1103/physrevlett.108.227001
64. Kasumov, A. Yu.; Deblock, R.; Kociak, M.; Reulet, B.; Bouchiat, H.; Khodos, I. I.; Gorbatov, Yu. B.; Volkov, V. T.; Journet, C.; Burghard, M. *Science* **1999**, *284*, 1508. doi:10.1126/science.284.5419.1508
65. van Dam, J. A.; Nazarov, Y. V.; Bakkers, E. P. A. M.; De Franceschi, S.; Kouwenhoven, L. P. *Nature* **2006**, *442*, 667. doi:10.1038/nature05018
66. Cleuziou, J.-P.; Wernsdorfer, W.; Bouchiat, V.; Ondarçuhu, T.; Monthieux, M. *Nat. Nanotechnol.* **2006**, *1*, 53. doi:10.1038/nnano.2006.54
67. Ingerslev Jørgensen, H.; Novotný, T.; Grove-Rasmussen, K.; Flensberg, K.; Lindelof, P. E. *Nano Lett.* **2007**, *7*, 2441. doi:10.1021/nl071152w
68. Eichler, A.; Deblock, R.; Weiss, M.; Karrasch, C.; Meden, V.; Schönenberger, C.; Bouchiat, H. *Phys. Rev. B* **2009**, *79*, 161407. doi:10.1103/physrevb.79.161407
69. Delagrangé, R.; Luitz, D. J.; Weil, R.; Kasumov, A.; Meden, V.; Bouchiat, H.; Deblock, R. *Phys. Rev. B* **2015**, *91*, 241401. doi:10.1103/physrevb.91.241401
70. Zazunov, A.; Levy Yeyati, A.; Egger, R. *Phys. Rev. B* **2011**, *84*, 165440. doi:10.1103/physrevb.84.165440
71. Peng, Y.; Bao, Y.; von Oppen, F. *Phys. Rev. B* **2017**, *95*, 235143. doi:10.1103/physrevb.95.235143
72. Brunetti, A.; Zazunov, A.; Kundu, A.; Egger, R. *Phys. Rev. B* **2013**, *88*, 144515. doi:10.1103/physrevb.88.144515
73. Szombati, D. B.; Nadj-Perge, S.; Car, D.; Plissard, S. R.; Bakkers, E. P. A. M.; Kouwenhoven, L. P. *Nat. Phys.* **2016**, *12*, 568. doi:10.1038/nphys3742
74. Leijnse, M.; Flensberg, K. *Phys. Rev. Lett.* **2011**, *107*, 210502. doi:10.1103/physrevlett.107.210502
75. Sticlet, D.; Bena, C.; Simon, P. *Phys. Rev. Lett.* **2012**, *108*, 096802. doi:10.1103/physrevlett.108.096802
76. Prada, E.; San-José, P.; Aguado, R. *Phys. Rev. B* **2012**, *86*, 180503. doi:10.1103/physrevb.86.180503
77. Prada, E.; Aguado, R.; San-José, P. *Phys. Rev. B* **2017**, *96*, 085418. doi:10.1103/physrevb.96.085418
78. Hoffman, S.; Chevallier, D.; Loss, D.; Klinovaja, J. *Phys. Rev. B* **2017**, *96*, 045440. doi:10.1103/physrevb.96.045440
79. Martín-Rodero, A.; Levy Yeyati, A. *J. Phys.: Condens. Matter* **2012**, *24*, 385303. doi:10.1088/0953-8984/24/38/385303
80. Balatsky, A. V.; Vekhter, I.; Zhu, J.-X. *Rev. Mod. Phys.* **2006**, *78*, 373. doi:10.1103/revmodphys.78.373
81. Zazunov, A.; Shumeiko, V. S.; Bratus', E. N.; Lantz, J.; Wendin, G. *Phys. Rev. Lett.* **2003**, *90*, 087003. doi:10.1103/physrevlett.90.087003

License and Terms

This is an Open Access article under the terms of the Creative Commons Attribution License (<http://creativecommons.org/licenses/by/4.0>), which permits unrestricted use, distribution, and reproduction in any medium, provided the original work is properly cited.

The license is subject to the *Beilstein Journal of Nanotechnology* terms and conditions: (<https://www.beilstein-journals.org/bjnano>)

The definitive version of this article is the electronic one which can be found at:
[doi:10.3762/bjnano.9.158](https://doi.org/10.3762/bjnano.9.158)